Applied Energy 267 (2020) 114781

Contents lists available at ScienceDirect

Applied Energy

journal homepage: www.elsevier.com/locate/apenergy

A comprehensive and fully predictive discrete methodology for volumetric solar receivers: application to a functional parabolic dish solar collector system

Jorge E.P. Navalho*, José C.F. Pereira

LAETA, IDMEC, Instituto Superior Técnico, Universidade de Lisboa, Av. Rovisco Pais, 1, 1049-001 Lisbon, Portugal

HIGHLIGHTS

- A methodology for fully predictive simulations of volumetric receivers is presented.
- A coherent coupling strategy between the solar flux and receiver models is developed.
- The solar flux model is applied from the light source to the internal receiver walls.
- Best practice guidelines for accurate predictions with this methodology are given.
- The performance of a volumetric receiver in a parabolic dish assembly is evaluated.

GRAPHICAL ABSTRACT

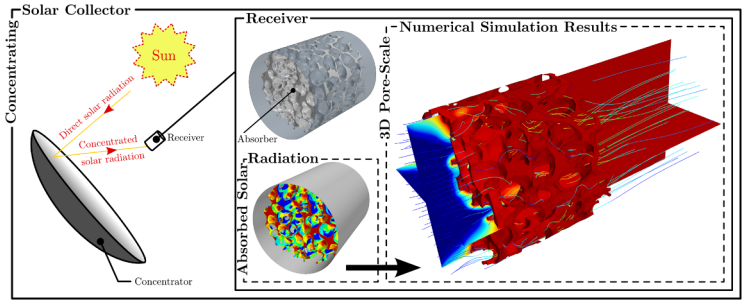

ARTICLE INFO

Keywords:
Concentrating solar power
Volumetric solar absorber
Parabolic dish
Ceramic foam
Pore-scale model
Volumetric effect

ABSTRACT

A comprehensive modeling approach is herein presented for accurate and reliable numerical predictions of the optical, hydrodynamic, and thermal performance of concentrating solar collector systems. The methodology is applied to investigate the performance of a particular and fully functional parabolic dish solar collector system fitted with a volumetric absorber (open-cell foam). At the receiver level, the methodology establishes a full and consistent coupling between the three-dimensional discrete hydrothermal model and the three-dimensional discrete solar flux model – the same receiver geometrical fidelity can be considered for both simulation stages. The receiver hydrothermal model relies on pore-scale numerical simulations of the heat transfer fluid flow, conjugate heat transfer, and radiative heat transfer. The collector solar flux model is based on the Monte Carlo ray tracing technique taking into account the solar insolation characteristics, the role of the concentrator device, and the detailed geometrical representation of the intricate absorber structure. Best practice guidelines for applying the current methodology are provided. The models comprising the overall methodology are validated against benchmark data. The results from the methodology application show specific absorber regions – namely, near the absorber front (irradiated) section – with relatively higher temperatures that are promoted by local geometric features of the absorber structure and are responsible to increase emission losses. This evidence could not be realized through the volume-averaging modeling approach. The results also support the inability of local thermal equilibrium models and the surface approach for the incoming concentrated solar radiation to accurately predict the receiver hydrothermal performance.

* Corresponding author.
E-mail addresses: jorge.navalho@tecnico.ulisboa.pt (J.E.P. Navalho), jcfpereira@tecnico.ulisboa.pt (J.C.F. Pereira).

https://doi.org/10.1016/j.apenergy.2020.114781
Received 31 August 2019; Received in revised form 17 February 2020; Accepted 28 February 2020
Available online 08 April 2020

1. Introduction

Solar energy harvesting for high-temperature heat – concentrating solar power (CSP) – applications has been the subject of intense research since the early 1970's following the first oil crisis [1–3]. Proved technologies for large-scale and centralized electricity production (based on parabolic troughs, solar towers, and linear Fresnel systems) have been deployed at the commercial level since the 1980's [4,5]. Recently, a higher level of competitiveness and dispatchability of this technology in relation to other renewable energy conversion technologies – viz., solar photovoltaics and wind power – is being achieved due to the thermal energy storage (TES) capabilities featured by new CSP plants [6,7]. These technologies offer a great potential for decarbonizing the energy economy [8].

Concentrating solar power technologies make use of solar receivers where the concentrated solar radiation is converted into thermal energy (useful energy) [9]. Volumetric receivers are a promising class of receivers commonly used for non-linear solar concentrator systems, such as the solar tower and parabolic dish CSP technologies (point-focus systems). Volumetric receivers are composed by porous structures (absorber matrix) through the pores of which the concentrated solar radiation – redirected from the concentrator devices – penetrates and a fluid passes under a forced convection flow regime. As the concentrated solar radiation penetrates within the absorber volume, a fraction of radiation is gradually absorbed by the solid structure, being transported as thermal energy to a heat transfer fluid (HTF) by convection. The high-temperature HTF from concentrating solar receivers can be delivered to downstream energy demanding applications (industrial process heat) or can be coupled either in an open- or closed-loop fashion to a power cycle block (conventional Rankine, Brayton, combined, or Stirling cycles) [10]. By promoting a volumetric heating instead of a surface heating – as in tubular receivers –, higher absorber temperatures can be displaced to the interior of the receiver pore structure, preventing long-wave thermal emission losses to the surrounding environment and improving the energy conversion efficiency – this phenomenon is the so-called volumetric effect [11,12].

Volumetric receivers have been extensively investigated by numerical simulations, particularly, in the last few years [13]. The main goals of these works consist in finding advanced absorber structures and suitable operating regimes to increase the solar radiation absorption and reduce heat losses from the receiver unit – improve the receiver optical and thermal performance [10,12]. The receiver performance characterization by numerical simulations is generally a common procedure prior to any prototyping and initial experimental investigations of improved or novel absorber designs. A large variety of models for the prediction of the receiver hydrothermal performance has been applied in the literature ranging from 1D (one-dimensional) continuum models – lumped models in radial and angular directions – (see, for instance, Refs. [11,14,15]) to 3D (three-dimensional) fully distributed and discrete (pore-scale) models [16]. The most common modeling approach has been based on the 2D (two-dimensional) or 3D volume-averaging local thermal non-equilibrium (LTNE) modeling formulation – see examples in Refs. [17–19]. According to this modeling strategy, the absorber thermal performance is governed by the coupled heat transfer behavior between continuum solid and fluid phases – absorber matrix and heat transfer fluid, respectively. (Local thermal equilibrium (LTE) models have been also applied in the literature – see Refs. [20,21] – but are generally not as suitable as LTNE models due to the large temperature deviations between the two phases that are observed mainly near the irradiated/inlet receiver section. Consequently, LTE models are known to predict excessive and unrealistic volumetric effects.) The heat transfer fluid flow within the receiver volume is predicted resorting to momentum balance equations that employ effective hydrodynamic external (empirical- or theoretically-derived) source terms – permeability and inertial resistance coefficients [22–24]. Effective thermophysical properties, such as thermal conductivities, specific heats, densities, and radiative properties are required being estimated in accordance with the respective intrinsic properties of the single phase and the volume fraction of each phase [25].

In volume-averaging LTNE models, heat transfer rates between solid and fluid phases strongly rely on the application of external correlations – derived from experimental measurements or from pore-scale numerical simulations – for the evaluation of convection heat transfer coefficients [26–28]. Moreover, since solar radiation transport and convection heat transfer are the dominant processes in solar-to-thermal energy conversion, the reliability and accuracy of such two-phase (heterogeneous) volume-averaging model predictions become highly sensitive to the values applied for the external heat transport coefficients. The same is equally true for the source terms of the momentum balance equations for an accurate prediction of the fluid flow behavior (and overall pressure drop) within the receiver unit. Some uncertainty and reserve in relation to the predictive capabilities exhibited by this class of models should be considered, specially for hydrothermal regimes of operation and geometrical parameters far from those that were considered at first instance to develop such transport correlations. Moreover, there is little awareness in the literature to the physical dimensions of the absorber volume – where the volume-averaging model equations are to be applied – in relation to the characteristic pore size of the structure. This is particularly critical for cases where the overall absorber dimensions are similar to the pore size dimensions (only a few cell units per volume are considered), which should strongly discourage the application of such correlations because they were derived under the basic assumption of a minimum representative elementary volume – several times higher (to be statistically representative of the entire structure) than the characteristic pore size [29,30].

Conversely to volume-averaging models, pore-scale models do not rely on external correlations neither on effective thermophysical parameters for the description of fluid flow and heat transfer phenomena. Instead, these models solve the Navier-Stokes equations for the fluid flow field solution within the pore network of the receiver (gas phase), and solve the conjugate heat transfer problem, coupling the energy balances of both solid and fluid phases without external – eventually, unsuitable – Nusselt number correlations [31]. These models are more computational demanding than volume-averaging models and require the digital reconstruction of the absorber complex pore network morphology – that can be acquired from different volume imaging techniques (e.g., magnetic resonance imaging and X-ray computer tomography) or developed from reconstruction algorithms. For such reasons, pore-scale models are not widely used for engineering purposes, namely for initial (preliminary) parametric and extensive investigations [32,16]. The micro-scale details of the fluid flow and heat transfer within the intricate absorber porous structure are resolved applying pore-scale models [33]. This kind of models allows to capture particular features of pore-scale phenomena that otherwise – with non-intrusive experimental measurement techniques – would be very difficult to get access [34]. The application of these models represents a great opportunity to shed light and gain physical insight (improved understanding) on some open and conflicting issues found in the literature, for instance, regarding the effect of foam geometrical properties (porosity and mean pore size) on the receiver thermal efficiency [17,19,35].

The role of solar insolation characteristics and concentrator devices on the receiver hydrothermal performance has been theoretically considered through two fashions: the surface approach; and the volumetric approach. The surface approach considers the absorption of the incoming concentrated solar radiation energy as a surface phenomenon lumped at the absorber irradiated (front) section. This approach is mainly applied along with volume-averaging receiver hydrothermal models [26,36,37] and is scarcely found in the literature – in comparison with the volumetric approach – due to the underlying limitations for high-accuracy predictions. (For dense absorber structures, the surface approach may eventually become more adequate but by definition this approach is unable of reflecting the volumetric effect.) On the other hand, according to the volumetric approach the incoming concentrated

solar radiation energy is absorbed continuously along the porous (extinction) volume of the absorber. The volumetric approach has been applied through the modified P_1 approximation [38,39], discrete ordinates method [40,15], two-flux approximation [11], or through exponential (phenomenological) laws [24,25,41]. Additionally, ray tracing methods considering continuum-scale [42,43] or discrete-scale [44,45] approaches for the receiver morphological representation are also frequently considered. The application of the surface and volumetric fashions requires a prior knowledge of the incident concentrated radiation flux distribution – and, preferably, the incident concentrated radiation angle distribution – at the receiver aperture section. This data can be calculated taking into account the performance of the reflector devices through Monte Carlo ray tracing (MCRT) techniques [39] or, simply, assumed as constant [18,26] or described by Gaussian distributions [23,38] in line with experimental estimates. Alternatively, the volumetric approach implemented with MCRT techniques can be applied following to a one-step (fully coupled) manner from the solar disc to the internal receiver walls. The application of MCRT methods embracing simultaneous all concentrating solar collector components comprises the most comprehensive procedure for modeling solar radiation transport and absorption [43,46,47].

Only a few direct pore-scale numerical simulations have been specifically conducted for the evaluation of the hydrothermal performance of volumetric solar receivers. Du et al. [48] have applied such a model approach to an open volumetric air receiver composed by an open-cell foam absorber reconstructed from computed tomography scans. The authors have decoupled the solar field concentrator role from the receiver performance by simply assuming an already concentrated and collimated incident solar radiation at the receiver front section and did not give any value for the receiver optical or thermal efficiency. By performing pore-scale numerical simulations in 10 ppi foams with different porosities, Du et al. [25] have recently developed a Nusselt number correlation taking into consideration typical operating conditions (realistic thermal boundary conditions) for volumetric solar absorbers. Zhu and Xuan [49] have applied a pore-scale model to evaluate the effect of porosity, incoming concentrated radiation incident angle, and receiver absorptivity with three types of structured packed bed volumetric solar receivers. However, instead of solving the conjugate heat transfer problem the model makes use of an external correlation for the interface heat transfer coefficient. For honeycomb absorber structures, Nakakura et al. [40] have analyzed five different channel inlet geometries with a 3D multi-channel discrete model and found potential performance benefits that were rationalized with lower shadowing effects on the channel internal walls. Cagnoli et al. [46] and Fend et al. [41] have applied 3D single-channel (pore-scale) models to investigate the effect of different honeycomb channel dimensions (edge length and wall thickness) on the hydrothermal absorber performance. Capuano et al. [50] have investigated an innovative and optimized volumetric solar receiver comprised by a pin-shaped inlet (irradiated) zone followed by an inner staggered honeycomb structure, through 3D discrete numerical simulations. The majority of these pore-scale numerical modeling studies have neglected the optical role of the solar concentrator on the hydrothermal receiver performance – an assumption on the incident concentrated solar radiation distribution has been commonly considered instead. Furthermore, in several works the solar radiation absorption along the absorber structure has been computed through simplistic approaches – such as the Beer's law – and radiative heat transfer modeling within the absorber volume has been ignored.

In this work, a comprehensive and fully predictive modeling approach is developed for accurate and reliable numerical performance characterization studies of concentrating collector solar systems. The current methodology is applied to investigate the optical, hydrodynamic, and thermal performance of a fully functional parabolic dish solar collector system with an open volumetric air receiver composed by a ceramic open-cell foam absorber. The 3D discrete geometric model for the absorber structure is considered in this study either for the evaluation of the absorbed solar radiation distribution and for the prediction of the hydrothermal performance. No assumption is required on the incoming concentrated solar radiation features since the directional radiation characteristics as well as the heat flux distribution at the receiver aperture section are completely predicted by the solar flux model. A data managing strategy to deal with the high morphological complexity details of the receiver is proposed in order to guarantee the coherent coupling between the solar flux (optical) model results and the receiver (hydrothermal) model. This strategy can be readily applied to combine available CFD (computational fluid dynamics) and optical simulation codes. The application of the current methodology only requires intrinsic properties of the collector system and solar insolation and receiver operating conditions. As far as the authors are aware, the current work is the first of its kind to deal with a complete and fully functional parabolic dish solar collector system (concentrator and receiver) resorting to pore-scale numerical models – to describe the hydrothermal performance of the receiver – and to a solar flux model based on the Monte Carlo ray tracing technique to take into account the solar insolation characteristics (solar model), the concentrator, and the detailed receiver internal structure on the absorbed solar power – without any averaging procedure to alleviate the solar flux calculations. A comprehensive preliminary investigation is herein addressed outlining the best practice guidelines while applying this methodology and covering a mesh independence study, a parametric investigation on the accuracy of the thermal radiative heat transfer model, and a validation procedure.

This document is organized as follows. The next section (Section 2) provides a brief description for the physical models of the solar and collector system that will be considered for the methodology application. Thereafter, Sections 3 and 4 present the mathematical and numerical modeling details, respectively, proposed to solve the overall concentrating solar collector problem. The results and ensuing discussion (including practice guidelines for accurate and reliable numerical predictions with the current methodology) are addressed in Section 5. This document ends in Section 6 with summary conclusions.

2. Physical models

2.1. Collector and solar systems

The concentrating solar collector system is composed by a concentrator (reflector) and a receiver. The concentrator collects and redirects beam (direct) solar radiation towards the receiver where the concentrated solar energy is absorbed by a solid matrix (absorber structure) and transferred to a flowing heat transfer (or working) fluid under a forced flow regime. According to this process, the conversion of solar energy to thermal energy is accomplished. In this work, the concentrator is an ideal parabolic dish and the solar receiver belongs to the volumetric class. Fig. 1 illustrates a schematic representation of the concentrating solar collector system. The supporting structures that hold the receiver in place – which are commonly attached to the concentrator – are neglected. The receiver symmetry axis is collinear with the parabolic dish axis (axis parallel to axis z) – no radial misalignment (eccentricity) is considered between the concentrator and receiver apertures. The receiver front (aperture) section is located at the focal plane of the parabolic dish concentrator. The concentrator focal length (f) and aperture radius (R_{aper}) – parameters shown in Fig. 1 and required for the geometrical definition of the parabolic dish – are equal to 3 and 0.2 m, respectively.

The sun shape effect – angular intensity distribution of direct sun rays along the solar disc – is modeled according to the pillbox distribution with a solar cone half-angle (θ_s) of 4.65 mrad. The sun position is set in the collector symmetry axis. A value of 1000 W m^{-2} is considered for the incident solar direct normal irradiation (DNI). Air is the heat transfer fluid as it is commonly considered in open (atmospheric) volumetric solar receivers.

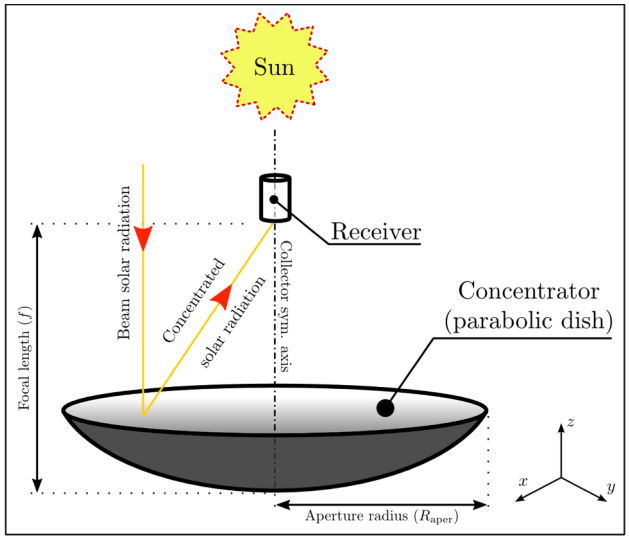

Fig. 1. Schematic representation of the concentrating solar collector system.

2.2. Volumetric solar receiver

The volumetric receiver is composed by the solar absorber and the corresponding supporting structure (tubular housing structure). The absorber structure corresponds to a ceramic (SiC) open-cell foam matrix. Fig. 2 depicts the physical model of the solar receiver and absorber. The absorber cellular structure has a cylindrical shape with a length and diameter equal to 20 and 25 mm, respectively. The absorber is fixed in the middle of a 30 mm long tube. In this study, the thickness of the tube wall is neglected. Fig. 2 specifies where the irradiated receiver section is

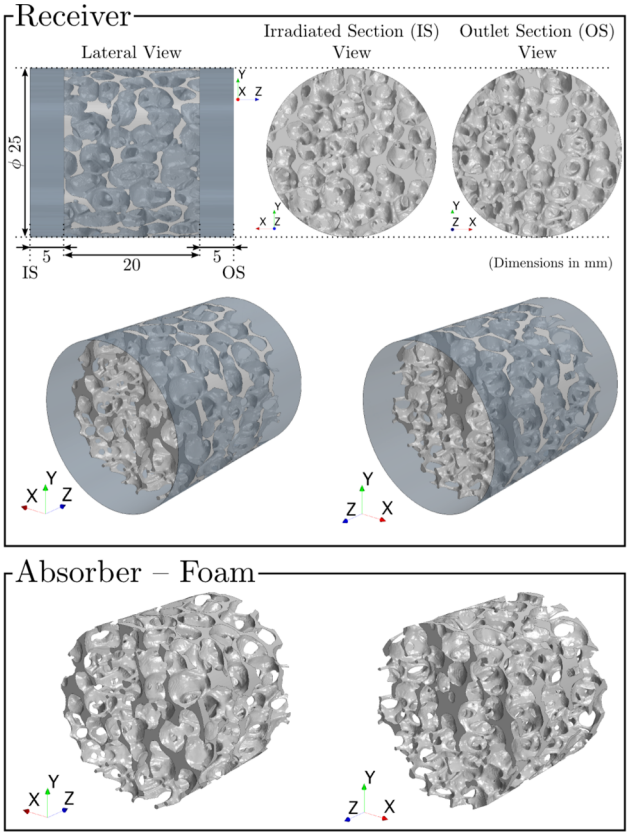

Fig. 2. Physical model (including dimensions) of the receiver unit and absorber structure.

Table 1
Geometrical characteristics of the open-cell foam absorber.

Parameter	Value
Cell density [ppi]	10
Porosity (ϕ) [%]	83
Specific surface area (a_V) [m^{-1}]	669
Strut diameter (d_{strut}) [mm]	0.7
Pore diameter (d_{pore}) [mm]	4.8

located – see the label "IS" on the top-left inset. The morphology of the foam absorber considered in this work was acquired by computed tomography scans of a real 10 ppi ceramic foam sample, with a voxel resolution of 70 μm, followed by a segmentation procedure (image processing techniques) carried out with the free and open-source software ITK-SNAP [51]. Table 1 lists the geometrical characteristics of the open-cell foam absorber. The open-cell foam porosity in Table 1 corresponds to the hydrodynamic effective – hydrodynamically relevant – porosity (macroscopic porosity). The foam ligaments are assumed as dense solid (not hollow) structures and, hence, the inner micro-porosity (strut porosity) is neglected and the total porosity becomes equal to the hydrodynamic porosity. The strut porosity – that depends mainly on the manufacturing procedure – is in general very low in relation to the hydrodynamic porosity (0.01% – 5%) [52,53] and it has been neglected in many literature works. d_{pore} corresponds to the inner pore diameter.

3. Mathematical models

3.1. Overall concentrating solar collector model: governing equations

The overall problem under consideration is herein handled with a single one-way coupling strategy between two sets of models: (a) the receiver fluid flow and heat transfer model – shortly, the receiver (hydrothermal) model; and (b) the collector solar flux model. The receiver model evaluates the fluid dynamics and thermal performance of the concentrating solar collector. The solar flux model feeds the receiver model with the contribution of the concentrated direct solar beams from the solar system, taking into account the optical and geometrical role of the concentrator system and receiver unit.

3.1.1. Receiver model

For pore-scale fluid flow and heat transfer simulations, the governing equations correspond to the conservation equations of mass, momentum, and energy (in both phases) in a continuum medium. This set of equations does not require external parameters (constitutive relations) for model closure as volume-averaging (continuum) models do, namely viscous and inertial permeability coefficients for the momentum source term, external heat transfer (convection) correlations for coupling the solid and fluid energy balance equations, and effective thermophysical properties.

The steady-state governing equations assuming laminar and incompressible fluid flow conditions and neglecting body forces and volumetric energy sources in a differential form read as follows – see Eqs. (1)–(4).

$$\nabla\cdot(\rho\mathbf{v}) = 0 \tag{1}$$

$$\nabla\cdot(\rho\mathbf{v}\otimes\ \mathbf{v}) = \nabla\cdot\boldsymbol{\sigma} \tag{2}$$

$$\nabla\cdot(\rho E\mathbf{v}) = \nabla\cdot(\mathbf{v}\cdot\boldsymbol{\sigma}) - \nabla\cdot(-k_f\nabla T_f) \tag{3}$$

$$\nabla\cdot(-k_s\nabla T_s) = 0 \tag{4}$$

Eqs. (1)–(4) correspond to the conservation equations of mass, momentum, energy in the fluid phase, and energy in the solid phase, respectively. In these equations, ρ, $\mathbf{v}$, $\boldsymbol{\sigma}$, E, k, and T are the fluid density, fluid velocity, stress tensor, fluid total energy per unit mass, thermal conductivity, and temperature, respectively. The subscripts f and s refer

to the fluid and solid phases, respectively. The stress tensor is given by Eq. (5), where p is the pressure and $\mathbf{T}$ the viscous stress tensor provided by Eq. (6). In Eq. (6), μ is the fluid dynamic viscosity.

$$\boldsymbol{\sigma} = -p\mathbf{I} + \mathbf{T} \tag{5}$$

$$\mathbf{T} = \mu[\nabla\mathbf{v} + (\nabla\mathbf{v})^T] - \frac{2}{3}(\nabla\cdot\mathbf{v})\mathbf{I} \tag{6}$$

The fluid total energy per unit mass is related with the fluid specific enthalpy (h) through Eq. (7).

$$E = h + \frac{1}{2}\|\mathbf{v}\|^2 - \frac{p}{\rho} \tag{7}$$

The fluid volume (air – heat transfer fluid) within the receiver void space is regarded as transparent (non-participant) to radiative heat transfer – the fluid medium does not emit, absorb, and scatter radiation [17,31]. In this work, the net radiation method (surface-to-surface radiative heat exchange model) [54] is employed to determine the net radiation heat flux from each surface to the surrounding receiver surfaces and external environment.

3.1.2. Solar flux model

The solar flux model is based on the Monte Carlo ray tracing technique. This method is widely employed by the concentrated solar energy research community owing to its simplicity, flexibility, scalability, accuracy, and capability of handling complex geometries [42,44,55]. This technique consists in tracking a large amount of individual rays from a specified emission source (solar disc) through, eventually, successive specular (in this work) reflections in the collector system until the absorption of rays takes place, at a particular collector surface, or the rays escape from the collector system realm. Whenever a ray impinges on a surface, a particular event probability for absorption and reflection is evaluated taking into account the optical properties and a random number generator.

3.2. Boundary and conjugate conditions – receiver model

At the inlet section of the receiver, uniform velocity and temperature distribution profiles are considered (see Eqs. (8) and (9), respectively). The flow direction is set normal to the receiver inlet section (Eq. (8)). At the receiver outlet section, a pressure outlet boundary condition establishing a zero static (gauge) pressure is applied (Eq. (10)) as well as a negligible fluid temperature gradient (Eq. (11)). (The reference pressure corresponds to the atmospheric pressure.) Unless otherwise stated, at the receiver internal walls, no-slip and impermeable boundary conditions are applied for the velocity field (Eq. (12)). The receiver external (tubular) surface is adiabatic ($\partial T/\partial n = 0$). At all wall boundaries an heat flux (energy source value) is applied. The local heat flux value (q'') has two contributions: one from the external (concentrated) solar radiation (q''_{ext}) – computed outside the framework of the receiver model, according to the solar flux model – and the other from the thermal radiation (thermal emission) within the porous media and between the internal receiver unit and the surrounding environment (q''_{int}) – see Eqs. (13) and (14), where $\mathbf{n}$ corresponds to the unit normal vector to the material interface. Eq. (15) states the temperature continuity across fluid-solid interfaces. (On the contrary, an heat flux jump is observed at the absorber surfaces due to the application of energy source values – see Eq. (14).) The boundary and conjugate conditions are summarized as follows.

1. Inlet section:

$$\mathbf{v} = v_{\text{in}}\,\vec{e_z} \tag{8}$$

$$T_f = T_{f,\text{in}} \tag{9}$$

2. Outlet section:

$$p = p_{\text{out}} \tag{10}$$

$$\nabla T_f\cdot\mathbf{n}_{\text{out}} = 0 \tag{11}$$

3. Wall boundaries:

$$\mathbf{v} = \mathbf{0} \tag{12}$$

3.1 Receiver external (outer) surface:

$$(k_f\nabla T_f\cdot\mathbf{n}) + q''_{\text{ext}} + q''_{\text{int}} = 0 \tag{13}$$

3.2 Fluid-solid interface (absorber surface):

$$(k_s\nabla T_s\cdot\mathbf{n}) = q''_{\text{ext}} + q''_{\text{int}} + (k_f\nabla T_f\cdot\mathbf{n}) \tag{14}$$

$$T_f = T_s \tag{15}$$

3.3. Thermophysical, optical, and radiative properties

The dynamic viscosity of air at moderate temperatures and atmospheric pressure is evaluated with the Sutherland's law with parameters taken from Ref. [56]. The ideal gas' law is considered to calculate the fluid mass density. The air specific heat and thermal conductivity are computed according to Eqs. (16) and (17), respectively, where T_f corresponds to the absolute air temperature. These equations were derived by polynomial fitting with the data gathered from Ref. [57] over the temperature range 250 − 1600 K. A maximum relative error below 0.4% and 2% is guaranteed applying Eqs. (16) and (17), respectively, in relation to the reference values (raw data).

$$c_{p,f}\,[\text{J kg}^{-1}\,\text{K}^{-1}] = 2.4422\times10^{-10}T_f^4 - 9.6767\times10^{-7}T_f^3 + 1.3251\times10^{-3}T_f^2 - 5.3090\times10^{-1}T_f + 1.0703\times10^{3} \tag{16}$$

$$k_f\,[\text{W m}^{-1}\,\text{K}^{-1}] = 3.4288\times10^{-11}T_f^3 - 9.1803\times10^{-8}T_f^2 + 1.2940\times10^{-4}T_f - 5.2076\times10^{-3} \tag{17}$$

For the thermal conductivity of the solid matrix (foam absorber solid fraction), the correlation reported in Ref. [58] for sintered α − SiC is herein applied. This correlation is presented in Eq. (18), where the solid temperature, T_s, is given in degrees Celsius. This correlation provides suitable values along the temperature range 0–2000 °C [58].

$$k_s\,[\text{W m}^{-1}\,\text{K}^{-1}] = \frac{52000\times\exp(-1.24\times10^{-5}T_s)}{T_s + 437} \tag{18}$$

In this work, foam strut walls are considered opaque surfaces. Due to the absence of detailed spectral properties for solar optical and thermal radiation heat transfer modeling purposes, every collector system wall is considered as a gray surface – i.e., no spectral selectivity is herein considered. Consequently, the receiver (absorber and housing structure) walls' solar absorptivity (α) is equal to its thermal emissivity (ϵ) – Kirchhoff's law. The emissivity of the SiC foam is considered equal to 0.93 [12]. For the receiver external wall (absorber metal housing surface), an emissivity equal to 0.3 is taken into consideration in agreement with previous works [17]. The concentrator surface reflectivity (ρ_{conc}) is equal to 0.9 in accordance with the literature [17,59]. The reflectivity values are assumed as averaged values over the entire range of possible incident angles and, consequently, these values are herein considered as independent of the angle of incidence [60–62].

4. Numerical models

4.1. Receiver model: fluid flow and heat transfer models

The receiver mathematical model is numerically solved through the commercial software package STAR-CCM+ (version 12.04), a finite volume multi-disciplinary simulation environment, currently owned, maintained, and distributed by Siemens. CAD modeling and computational domain discretization (mesh generation) are also carried out within the capabilities of this package. The fluid flow governing equations (Navier-Stokes equations) are solved with the built-in segregated flow solver that makes use of the SIMPLE algorithm. The segregated fluid temperature solver is applied to evaluate the fluid total energy equation considering the temperature as the solved variable. A second-order upwind discretization scheme is adopted for evaluating convective fluxes. The heat transfer between the fluid and solid phases within the receiver volume is solved through a conjugate – coupled or adjoint – formulation (conjugate heat transfer). Such an approach is required once each phase is governed by a different balance equation. This procedure allows to determine the temperature and heat flux distribution at the fluid-solid interface without resorting to externally derived convection heat transfer coefficients.

Thermal radiative heat transfer numerical modeling is accounted for through a native implementation of the net radiation method available in the commercial code STAR-CCM+. The required view factors are evaluated through a deterministic Monte Carlo approach that requires a specified number of rays. The rays are emitted from the center of each patch (individual surface) towards the enclosing space being traced until they intersect another patch. The specified number of rays controls the view factors accuracy.

4.2. Solar flux model and receiver model coherent coupling

The free and open-source MCRT software Tonatiuh (Version 2.2.4) [63] is applied for the calculation of the solar irradiation absorbed power on the collector surfaces. The procedure employed for computing the absorbed solar flux distribution on the irradiated receiver surfaces is briefly described in Fig. 3. The current approach allows to establish a one-to-one correspondence between the boundary cell faces of the pore-scale fluid flow and heat transfer model (receiver model) and the individual surfaces considered for MCRT model simulations.

The coupling procedure is initiated after the generation of a suitable mesh geometry within the framework of the receiver model. All mesh details regarding the receiver computational regions whose boundaries are exposed to solar radiation can be exported from the STAR-CCM + environment, however only in a binary format. The software STAR-CD (Version 4.14.010, developed by CD-adapco) was employed to handle the binary mesh file appropriately in order to generate ASCII plain text files (.bnd, .cel, and .vrt files) with all mesh features. Consequently, from the .bnd file, it is possible to determine the PROSTAR ID of each boundary cell and the corresponding boundary cell face(s), and finally, with such information using the data from the .cel file, the ID of each boundary cell face vertex is extracted. The coordinates of all vertices are gathered from the .vrt data file. At the end of this procedure, for each boundary cell face exposed to solar irradiation, the PROSTAR FACE ID is extracted as well as the coordinates of its composing vertices.

This data is employed to generate the composite foam surface for MCRT model simulation. The CAD_Shape surface import mode available in Tonatiuh was considered for defining each individual surface – through the STereo Lithography (STL) file format – that corresponds to each boundary cell face. The label assigned for each individual surface defined in the Tonatiuh source file is the PROSTAR FACE ID of the corresponding boundary cell face. This procedure is of paramount importance for the solar flux model post-processing stage, namely for importing the solar flux model results to the receiver model. This is because the same surface in both modeling environments has the same ID/label, which facilitates the import process to the receiver model, in such a way that no boundary cell face is left behind during the whole procedure (coherent coupling). FORTRAN programming was employed to generate the extensive source files for Tonatiuh, with all data required for setting up the simulation – geometrical and optical properties of the concentrator and receiver surfaces and parameters for the solar model definition – and to create the script file for running the simulation. The raw data from Tonatiuh's simulations (enclosing the path taken by each numerical ray within the solar collector system) was post-processed resorting to Python scripting. Finally, the data import procedure to the receiver model was performed with externally coded functions (written in FORTRAN) that were coupled to the receiver simulation model developed within the STAR-CCM+ framework.

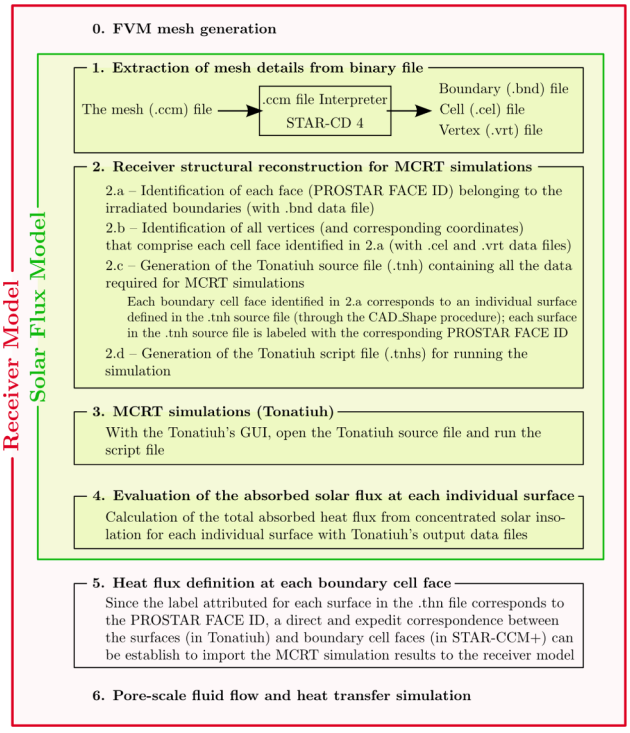

Fig. 3. Methodology applied for coupling the receiver pore-scale model and the solar flux model.

5. Results and discussion

This section includes a mesh independence study on the receiver hydrothermal numerical solution (Section 5.1), an investigation on sensitive parameters for the thermal radiative heat transfer model performance (Section 5.2), a validation procedure for the receiver and solar flux models (Section 5.3), and finally, a detailed analysis on the optical and hydrothermal performance of a particular, completely functional, solar collector system (Section 5.4).

5.1. Mesh independence study

Different meshes were generated for performing a mesh independence study on the numerical results in order to ensure that the results are independent from the domain discretization (mesh). The most adequate mesh – for which negligible differences are observed in relation to a more refined one – is selected for further simulations. The current mesh independence study is conducted at three different stage levels. The first stage analyses the effect of the mesh at capturing the geometric features of the absorber such as porosity and specific surface area – mesh independence study on the geometric fidelity of the

absorber structure. The second and third stages consider the mesh influence on primary solution fields at isothermal conditions and adiabatic conditions, respectively.

The computational domain corresponds to the physical model presented in Fig. 2 with the addition of two tubular (cylindrical) extruded regions – with the same diameter as the receiver external wall –, one placed upstream and the other downstream the receiver region. The tubular (embedding) regions are included to avoid the application of unsuitable hydrodynamic and thermal boundary conditions at the inlet and outlet receiver sections. Therefore, spurious solutions are prevented, flow structures are retained near the entrance and exit receiver sections, and the numerical convergence behavior is improved [30]. This procedure is commonly applied in the literature – see, for instance, Refs. [52,34,33]. For the upstream and downstream undisturbed cylindrical regions, a length of $0.5D$ and $3D$ were considered, respectively, where D corresponds to the receiver external diameter (equal to 2.5 cm). (The tubular external surface of the upstream (inlet) region is not considered as a physical boundary and, consequently, free-slip (frictionless) and adiabatic boundary conditions are therein applied, as well as, a transmissivity value equal to one – transparent surface for radiative heat transport purposes). The thickness of the outlet cylindrical zone (equal to $3D$) was adequate to prevent velocity and pressure fluctuations as well as backflow issues during the numerical convergence path, at the computational model exit section. Backflow at the exit section can be developed due to a negative pressure at the absorbers' wake in relation to the gauge pressure fixed at the exit section (pressure outlet boundary condition).

Polyhedral cells were applied for discretizing the regions corresponding to solid domain (absorber material) and fluid space belonging to the receiver physical model. For every developed mesh, a layer of prismatic cells was considered at the interface between solid and fluid regions, immersed in the fluid side. The cells in the inlet and outlet tubular regions were developed by extrusion from the polyhedral cells generated in the central region (within the receiver region), considering 25 and 150 layers for the upstream and downstream tubular regions, respectively, along with a stretching ratio equal to two.

A total of 12 meshes were generated in this study. Table 2 lists the cell counts in the fluid and solid regions for each mesh. For the fluid region, Table 2 shows the number of cells in the porous region (region comprising the physical model of the receiver according to Fig. 2). Meshes A–G, H-2, and I–J were developed with the same set of specifications expect the mesh base size (which, consequently, gives rise to a different total number of cells). These meshes are listed in Table 2 by an ascending order of the total number of cells. Meshes H-1, H-2, and H-3 were created considering a different number of prism layers – two, five, and eight for meshes H-1, H-2, and H-3, respectively –, while keeping

Table 2
Number of cells (in millions) for each mesh in different regions. All meshes have five layers of prismatic cells except meshes H-1 and H-3 which have two and eight, respectively.

Mesh	Fluid Region		Solid	Total
	Porous Region	Total	Region	
A	1.04	1.22	0.17	1.39
B	1.54	1.80	0.26	2.06
C	2.55	2.97	0.45	3.42
D	3.59	4.17	0.64	4.81
E	5.33	6.17	0.95	7.12
F	10.54	11.96	1.98	13.94
G	13.51	16.51	2.22	18.73
H-1	12.82	17.81	2.41	20.22
H-2	16.48	21.74	2.41	24.15
H-3	20.13	25.67	2.41	28.08
I	18.86	25.74	2.60	28.34
J	20.93	29.02	2.83	31.85

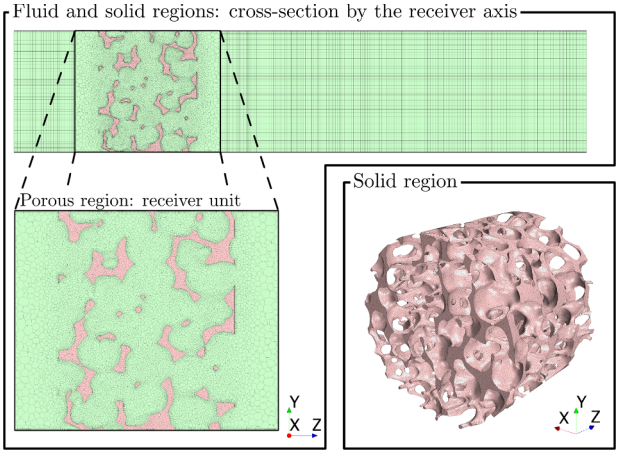

Fig. 4. Representation of different mesh features. (Mesh B in consideration – see Table 2.).

constant the remaining mesh parameters. Fig. 4 depicts several geometric features considered for the meshes under consideration.

Fig. 5 presents the relative errors of porosity and specific surface area calculated for different meshes and taking as reference mesh J – finest mesh with about 32 million cells. From mesh F to mesh I, the relative errors of porosity and specific surface area become negligible (below 0.15%). A decrease on cell size contributes to enhance the geometrical fidelity of the mesh geometry in relation to the physical model of the absorber. For a coarse mesh, the smallest geometric details of the physical model may not be accurately resolved – the smallest pores and cell windows of the original foam geometry may become occluded by the solid mesh which leads to a decrease of porosity and specific surface area. The number of prismatic cells does not affect the discretization of the interface between the solid and fluid domains; therefore, meshes H-1, H-2, and H-3 feature equal values for the geometric properties under consideration and equal relative errors on the porosity and specific surface area – for this reason only mesh H-2 is presented in Fig. 5.

5.1.1. Isothermal conditions: hydrodynamic behavior

For this set of simulations, the air superficial velocity (v_{in}) and temperature ($T_{f,in}$) were uniform at the inlet section and equal to 0.1 m s^{-1} and 300 K, respectively. A constant pressure at the outlet (p_{out}) was also considered.

Fig. 6 presents the pressure drop relative error computed for different meshes. The pressure drop was evaluated over the 30 mm receiver length. The friction on the receiver tubular enclosing walls has a minor contribution on the pressure drop over the absorber. Relative

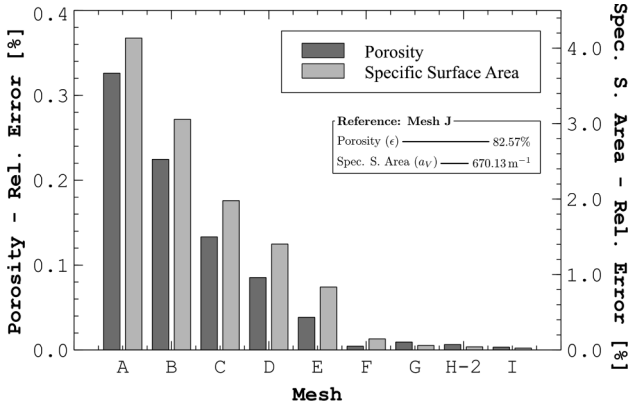

Fig. 5. Porosity and specific surface area relative errors determined for different meshes in relation to the corresponding values obtained with mesh J.

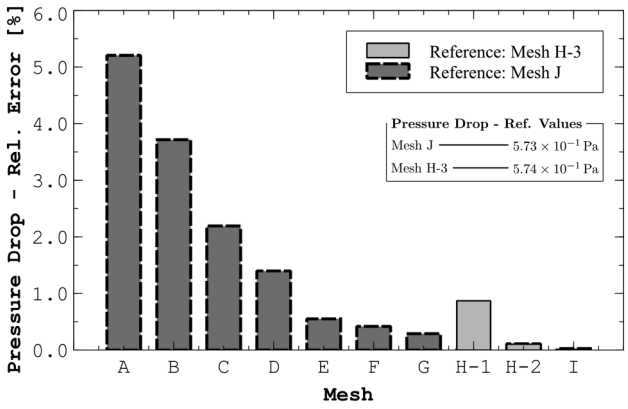

Fig. 6. Relative errors for the pressure drop along the absorber length determined for each mesh.

errors for meshes A–G, H-2, and I (meshes H-1 and H-2) were computed considering mesh J (mesh H-3) as reference. Fig. 6 shows that as the mesh cell count and number of prism layers increase a decrease in the pressure drop relative errors is observed. In particular, for mesh H-2 a relative error of 0.11% and 0.10% is calculated in relation to mesh J and mesh H-3, respectively.

Figs. 7a and 7b present velocity magnitude profiles for the reference meshes (mesh H-3 and mesh J) and relative errors of velocity magnitudes for different meshes in relation to the reference ones, respectively, along the axial direction of the receiver unit. The velocity magnitude at each receiver axial position corresponds to the average value over the entire transversal cross-section. In Fig. 7a et seq., the inlet section of the absorber (foam matrix) is located at the axial position (z) equal to 0. In Fig. 7a, similar results are observed for meshes H-3 and J. In Fig. 7b, the relative errors are more significant near the absorber inlet section ($z \approx 0$ cm), middle of the receiver ($z \approx 1$ cm), and at about 1 cm downstream the absorber outlet section ($z \approx 3$ cm) – absorber's wake. The same trend as before is herein registered: the relative error decreases with the cell count. For mesh H-2, the average and maximum relative errors are lower than 0.012% and 0.070%, respectively, taking as reference either mesh H-3 or mesh J.

5.1.2. Adiabatic conditions: hydrodynamic and thermal behavior

In this case, a constant heat flux is applied at the inlet (front face), internal, and outlet (rear face) surfaces of the absorber. The inlet conditions (fluid superficial velocity and temperature) are the same as those considered for the previous isothermal model simulations. The heat flux value was evaluated through an energy balance taking into account the actual air mass flow rate, inlet temperature, air thermophysical properties, and total absorber surface area, in such a way that the outlet gas temperature would be equal to 900 K. A total heat transfer rate value of about 36.5 W was calculated and applied at the absorber walls. The external walls of the receiver are set as adiabatic surfaces in accordance with the boundary conditions (see Section 3.2).

Fig. 8a presents the gas and solid axial temperature profiles for the reference meshes (meshes H-3 and J) and Fig. 8b shows the relative errors of gas temperature profiles along the axial direction of the receiver. The temperatures were evaluated as a surface average over the corresponding region (solid or fluid) of the cross-section at each receiver axial position. In Fig. 8a, negligible differences are perceived between the thermal profiles of each reference mesh. Fig. 8b shows that the maximum relative errors are observed at the inlet section of the absorber. A remarkable decrease of the relative errors near the absorber inlet section is observed as the cell density increases. For mesh H-2, a maximum relative error below 0.027% and 0.024% is reported in relation to mesh J and H-3, respectively. The relative errors concerning the solid temperature profiles were also computed (not shown herein). For each mesh, the maximum and average relative errors are lower for

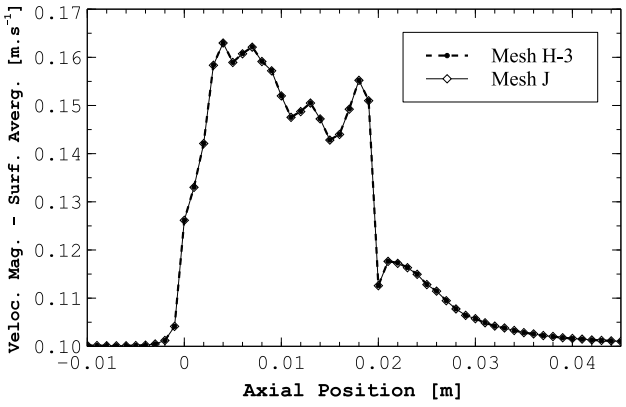

(a)

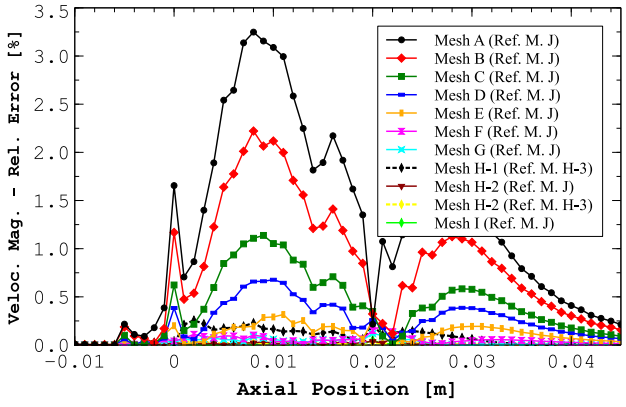

(b)

Fig. 7. Performance of each mesh for the calculation of the velocity field: (a) velocity magnitude profiles along the receiver axial coordinate for meshes H-3 and J; and (b) relative errors of velocity magnitudes for different meshes.

the solid temperature than for the gas temperature profiles. Although not directly relevant for the current mesh independence study, the pressure drop along the receiver equals to 2.37 and 2.38 Pa for mesh J and mesh H-3, respectively. The fourfold pressure drop increase in relation to the isothermal pressure drop values (see Fig. 6) is related to the fluid viscosity increase with temperature.

The results from the mesh independence study – on the absorber geometrical properties and on the hydrodynamic and hydrothermal performance of the receiver – support the selection of mesh H-2 as a suitable mesh for performing the forthcoming numerical simulations. The absorber physical model geometrical fidelity and numerical model results computed with mesh H-2 are similar to the geometrical fidelity and results computed with meshes having higher cell densities and more layers of prismatic cells.

5.2. Radiative heat transfer model

The accuracy of view factors strongly relies on the number of rays dispatched from each patch (see Section 4.1). Therefore, the sensitivity of the net radiation heat fluxes to the number of beams is herein investigated in order to establish an adequate value for further simulations. Although it is possible to define a ratio between boundary cell faces and patches, in such a way that each patch comprises a large number of cell faces – to alleviate numerical calculations (however at an expense of accuracy) –, in this work, each cell face represents an independent patch. This setting represents, simultaneously, the most accurate and expensive practice.

The temperature field solution computed in Section 5.1 with the

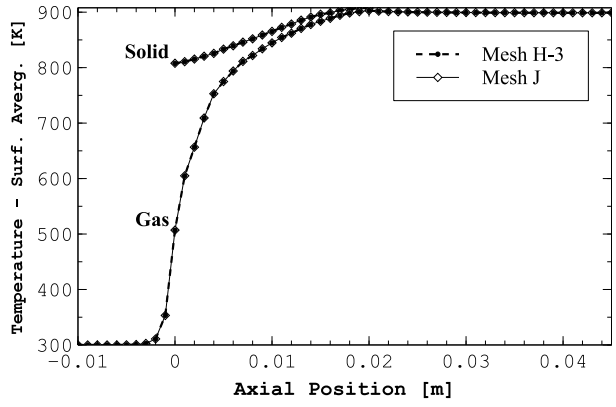

(a)

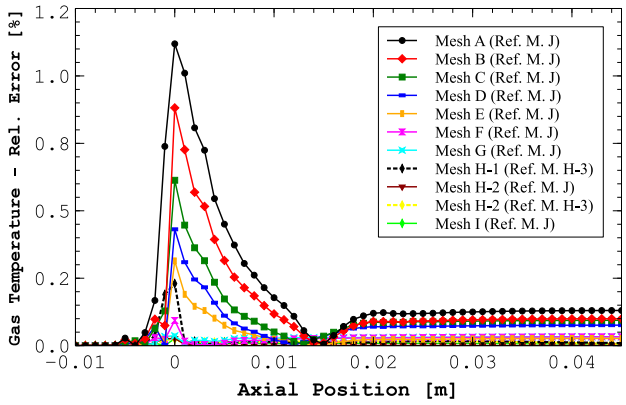

(b)

Fig. 8. Performance of each mesh for the calculation of the temperature distribution: (a) gas and solid temperature profiles along the receiver axial coordinate for meshes H-3 and J; and (b) relative errors of gas temperatures for different meshes.

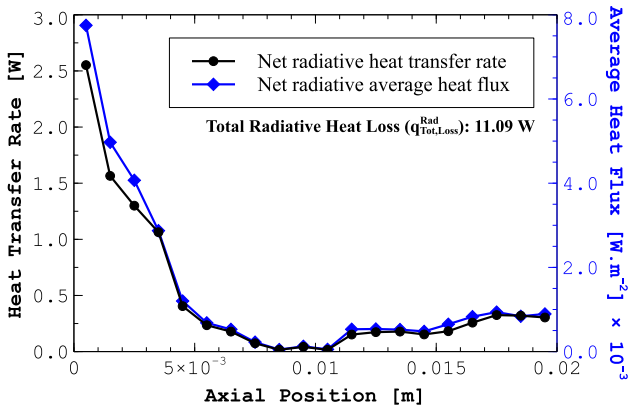

(a)

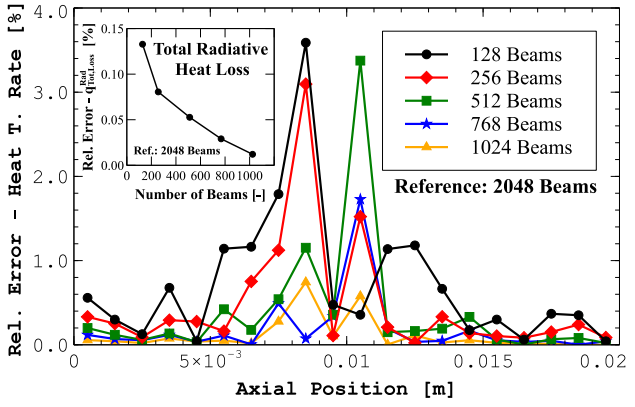

(b)

Fig. 9. Effect of the number of beams in the performance of the radiative heat transfer model: (a) net radiative heat transfer rate and average heat flux along the absorber axial coordinate evaluated with 2048 beams; and (b) relative errors for the net radiative heat transfer rate profiles computed with different number of beams in relation to the solution computed with 2048 beams. The inset of (b) presents the relative error of the total radiative heat loss from the absorber walls for a different number of beams.

mesh selected from the mesh independence study is herein applied to evaluate the effect of the number of beams on the radiation model results. Figs. 9a and 9b present the net radiative heat transfer rate profiles calculated with 2048 beams and the relative errors of such profiles calculated with a lower number of beams, respectively. A positive heat transfer rate in Fig. 9a implies a local radiative heat loss from the absorber. High values near the entrance section of the absorber are justified because the receiver inlet section corresponds to an open boundary to the surrounding environment at a temperature of 300 K. Near the exit section of the absorber the radiative heat losses also increase because the absorber walls are exposed to downstream manifolds at a slightly lower temperature (outlet gas temperature). At the middle of the absorber, minimal radiative heat losses are observed due to similar temperatures of neighboring absorber walls and to the optical thickness of the medium that hinders radiative heat exchange between local surfaces and surfaces located at higher distances, such the external environment surfaces (inlet receiver section).

Fig. 9b shows a decrease of the average relative error upon increasing the number of beams. For 1024 beams, an average and maximum relative errors of 0.11% and 0.74%, respectively, are registered. The relative error of the total radiative heat loss from the absorber walls computed with 1024 beams is about 0.01% in relation to the value calculated with two times the number of beams. These values support the selection of 1024 beams for computing the radiative heat transfer rates in the upcoming simulations.

5.3. Model validation

The performance of the receiver and solar flux models is herein compared against benchmark data gathered from the literature. For validation purposes, the receiver unit operation is carried out under isothermal and non-isothermal conditions in order to evaluate the hydrodynamic (fluid flow) and hydrothermal (fluid flow and heat transfer) performance, respectively.

5.3.1. Receiver model

Before considering pressure drop values (and correlations) from the literature as benchmark data for the current study, an initial investigation has to be conducted to ensure that the current absorber and pore dimensions allow the treatment of the overall media as a representative elementary volume (continuum – homogeneous – medium approach). If the overall dimensions of the absorber were not enough to guarantee such an approach then a comparison with literature data – obtained typically under the assumption of continuum media – should not be performed due to the inherent lack of reliability. A similar procedure suggested in Ref. [30] is herein followed.

Figs. 10a and 10b present the porosity and specific surface area for five sets of elementary volume (EV) units (EV-1 to EV-5), as a function of the EV characteristic length. A cylindrical shape for each EV is considered with the characteristic length (l_{EV}) equal to the EV radius

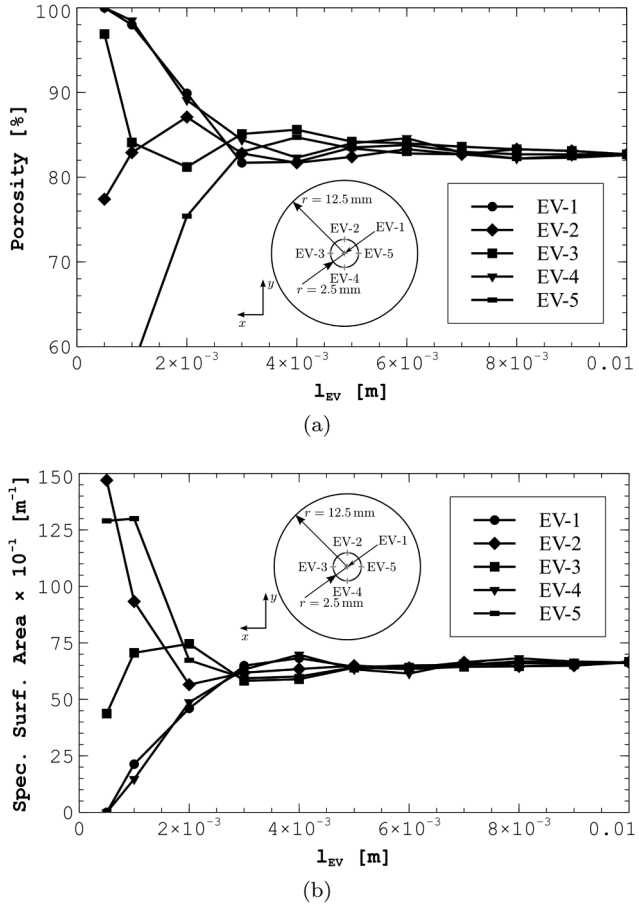

Fig. 10. Effect of the characteristic length (volume of the elementary units) on the unit geometrical parameters: (a) porosity; and (b) specific surface area. The insets in these figures show the central location for each elementary volume in the plane *xy*. The central position for all EVs are located in the *z* mid-plane.

and half EV height. A different central (starting) position – from where the volume of EV units is successively enlarged upon increasing l_{EV} – was considered for each EV set (see the insets of Figs. 10a and 10b). The results show that the geometric features of the EV, namely porosity and specific surface area become free from significant fluctuations as l_{EV} increases. This behavior is noticed even before l_{EV} equals 0.01 m. These results strongly suggest that the overall absorber can be regarded as a continuum medium and literature data can be readily used as benchmark.

Table 3 presents the pressure drop per unit bed (absorber) length computed at a constant temperature of 300 K and for an inlet (superficial) velocity of 0.1 m s^{-1}. In the numerical calculations for the determination of the pressure drop per unit bed length, free-slip boundary conditions were applied at the receiver external tubular walls. This procedure is commonly adopted in the literature – see, for instance, Refs. [52,34] – to avoid the contamination (falsification) of the results with external components, namely at lower superficial velocities. Nevertheless, if a higher volume for the sample were used (as it is usual in experiments), the effect of the fluid friction on the receiver external walls would be marginal on the overall pressure drop. The benchmark pressure drop value for the hydrodynamic conditions under consideration was calculated according to the Forchheimer equation fed with viscous and inertial permeability parameters evaluated with the correlations provided in Ref. [64]. The comparison between the present and reference pressure drop values leads to a relative error of about 6%, which is considered as a highly acceptable error in the literature related to the hydrodynamic characterization of open-cell foams – see, for instance, Ref. [65].

Table 3
Comparison between the pressure drop per unit bed length calculated in this work and evaluated with literature data.

	$\Delta p/\Delta l$ [Pa m^{-1}]
Present work	26.32
Ref. [64]	24.74

The performance of the receiver model under non-isothermal conditions (coupled fluid flow and heat transfer) is also herein compared against reference data in terms of local convection heat transfer coefficients. The simulation model results from the mesh independence study (Section 5.1) are herein considered for this purpose. Local convection heat transfer coefficients (h_{conv}) are computed according to Eq. (19), where q'' corresponds to the heat flux from the absorber surface to the bulk fluid stream, T_s is the solid temperature, and T_m is the mean (bulk) fluid temperature. T_m is calculated with Eq. (20) in agreement with Refs. [52,57,66].

$$h_{conv} = \frac{q''}{T_s - T_m} \tag{19}$$

In Eq. (20), h is the fluid specific enthalpy and $\mathbf{n}$ ($= 1\vec{e}_z$) is the unit vector aligned with the receiver symmetry axis (axis *z*). Thus, the numerator and denominator of Eq. (20) correspond to the integration of the enthalpy advection rate and to the mass flow rate, respectively, over the transversal cross-section. The temperature T_m is calculated in accordance to the corresponding mean enthalpy value (h_m). The integrals are performed over the fluid phase of the receiver transversal cross-sections.

$$h_m(T_m) = \frac{\int \rho(\mathbf{v}\cdot\mathbf{n})h dA}{\int \rho(\mathbf{v}\cdot\mathbf{n}) dA} \tag{20}$$

Fig. 11 presents the comparison between profiles of the local convection heat transfer coefficient along the receiver length obtained in this work and calculated according to two Nusselt number correlations developed for open-cell foams and widely applied in the literature – correlations reported in the Refs. [67] (Giani et al., 2005) and [64] (Garrido et al., 2008). Fig. 11 shows that the convection heat transfer coefficients evaluated in this work are well within the typical range of values reported in the literature.

The hydrodynamic and hydrothermal performance of the receiver model is in accordance with reference data and, consequently, the receiver model is validated.

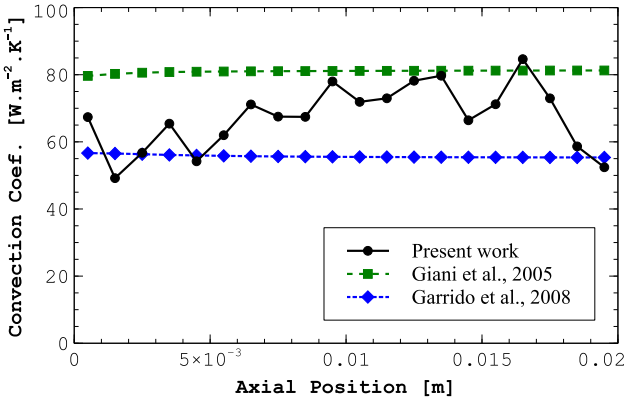

Fig. 11. Comparison between local convection heat transfer coefficients along the receiver main flow direction obtained in this work against the values evaluated from literature correlations.

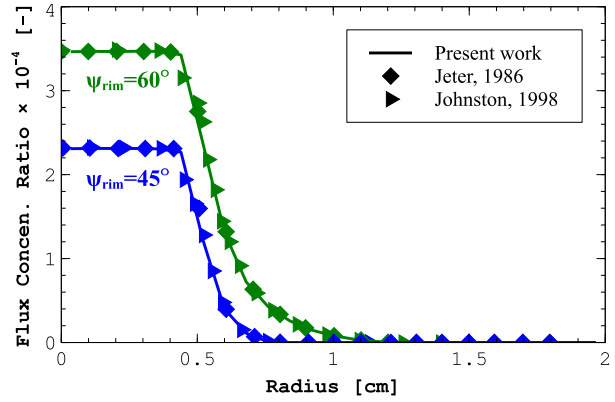

(a)

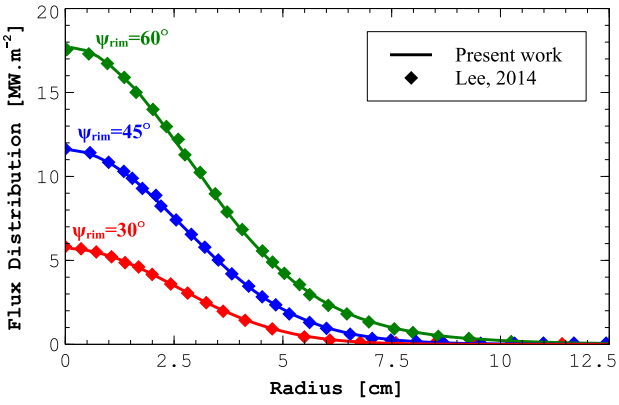

(b)

Fig. 12. Comparison of MCRT simulation results computed with Tonatiuh against reference values on the concentrator focal plane: (a) ideal parabolic dish ($\rho_{conc} = 1$, no optical errors) with $f = 1$ m for two rim angles (45 and 60°); and (b) parabolic dish with $f = 5$ m, $\rho_{conc} = 1$, and $\sigma_s = 2$ mrad for three rim angles (30, 45, and 60°).

5.3.2. Solar flux model

The solar flux model results computed with the MCRT software Tonatiuh are herein compared with benchmark data evaluated by numerical means and gathered from the literature. Two cases for the solar flux model validation are considered. In both cases, the main goal is the evaluation of the solar flux distribution on the focal plane of a parabolic dish concentrator that is exposed to direct solar radiation. Figs. 12a and 12b present the comparison between the actual results computed with Tonatiuh and the reference results for the two cases. Particularly, in Fig. 12a an ideal surface is considered for the parabolic dish, whereas in Fig. 12b the parabolic dish surface has a non-negligible slope error (σ_s). The benchmark data for the results in Figs. 12a and 12b were gathered from Refs. [68] (Jeter, 1986) and [69] (Johnston, 1998) and Ref. [70] (Lee, 2014), respectively. For both cases, different dimensions were considered for the concentrator. Figs. 12a and 12b show a very good agreement between Tonatiuh results and benchmark data. Therefore, the solar flux model is validated.

5.4. Collector optical and receiver hydrodynamic and thermal performance: detailed analysis

In this section, the full optical and hydrothermal performance characterization of the concentrating solar collector system introduced in Section 2 is conducted. According to the coupling methodology, a specific receiver mesh geometry – developed within the receiver model framework – is employed for the reconstruction of the irradiated surfaces for MCRT model simulations (see Section 4.2). The solar flux model procedure allows to use the selected mesh for the receiver pore-scale fluid flow and heat transfer model simulations. However, the level of mesh refinement (geometric definition) that is required for the receiver model may be dramatically higher than that required for the solar flux model. In this work, the previously developed meshes A and E (see Section 5.1) are herein applied for the reconstruction of the receiver geometrical model within the MCRT model framework. The number of boundary cell faces that are exposed to concentrated solar radiation (directly and after successive reflections) for each mesh is given in Table 4. The large majority of cell faces belongs to the definition of the complex absorber pore structure (absorber walls). The remaining cell faces define the external tubular receiver surface that encloses the absorber foam matrix. Mesh E is composed by about four times more boundary cell faces than mesh A. If mesh H-2 (mesh selected for receiver pore-scale hydrothermal model simulations) were taken as reference to the solar flux model, more than 1.2 million boundary cell faces would have to be considered as independent surfaces for MCRT model simulations.

Table 4
Number of independent surfaces that comprise the overall receiver structure within the MCRT model framework of simulations.

Surfaces	Number of Boundary Cell Faces	
	Mesh A	Mesh E
Absorber walls	131 421	510 866
Receiver tubular wall	18 708	56 490
Total receiver walls	150 129	567 356

The effect of the number of independent (individual) surfaces for the overall receiver geometrical definition and the number of rays from the solar source on the solar flux model results is addressed in Figs. 13a–c. Firstly, Fig. 13a shows for mesh E with 100 million rays the solar irradiation heat transfer rate profiles on the absorber walls along the receiver axial direction. (By “solar irradiation heat transfer rate” it is meant the net (absorbed) heat transfer rate from solar irradiation on the receiver surfaces.) The solar flux model computation time was about 23 h in 32 Intel® Xeon® Processor E5-2650 threads. (The running time increases for higher surface reflectivities. For instance, if the absorber surface emissivity were equal to 0.65 – instead of 0.93 – the computation time would increase to about 28.5 h.) The solar irradiation heat transfer rate decreases as the distance from the irradiated (front) receiver section increases. The local peaks observed in the interior of the absorber structure are related with the successive rows of pores whose surfaces are particularly exposed to solar radiation. From the middle of the absorber ($z = 0.01$ m) up to the outlet (rear) absorber section ($z = 0.02$ m), negligible solar radiation absorption is accounted for (less than 3% of the total solar absorbed power).

Fig. 13b compares the MCRT simulation results evaluated with mesh A and mesh E with 100 million rays, through absolute errors of the solar irradiation heat transfer rate axial profiles on the absorber walls. The errors are higher near the irradiated section and, generally, decrease towards the outlet section. The total solar irradiation heat transfer rate on the absorber walls is equal to 87.01 and 87.75 W for mesh E and mesh A, respectively. Fig. 13c presents the effect of the total number of rays on the solar irradiation heat transfer rate profiles over the absorber surfaces (mesh E) through relative errors computed in relation to the results presented in Fig. 13a (results evaluated with 100 million rays). The objective is to evaluate the sensitivity of the number of rays on the results, in order to select an appropriate total number which allows to obtain statistically meaningful results. Along the first quarter of the absorber length, very low relative errors are observed for all total number of rays considered. The differences become more striking from the middle of the receiver up to the outlet section. In general, as the total number of rays increases the maximum and

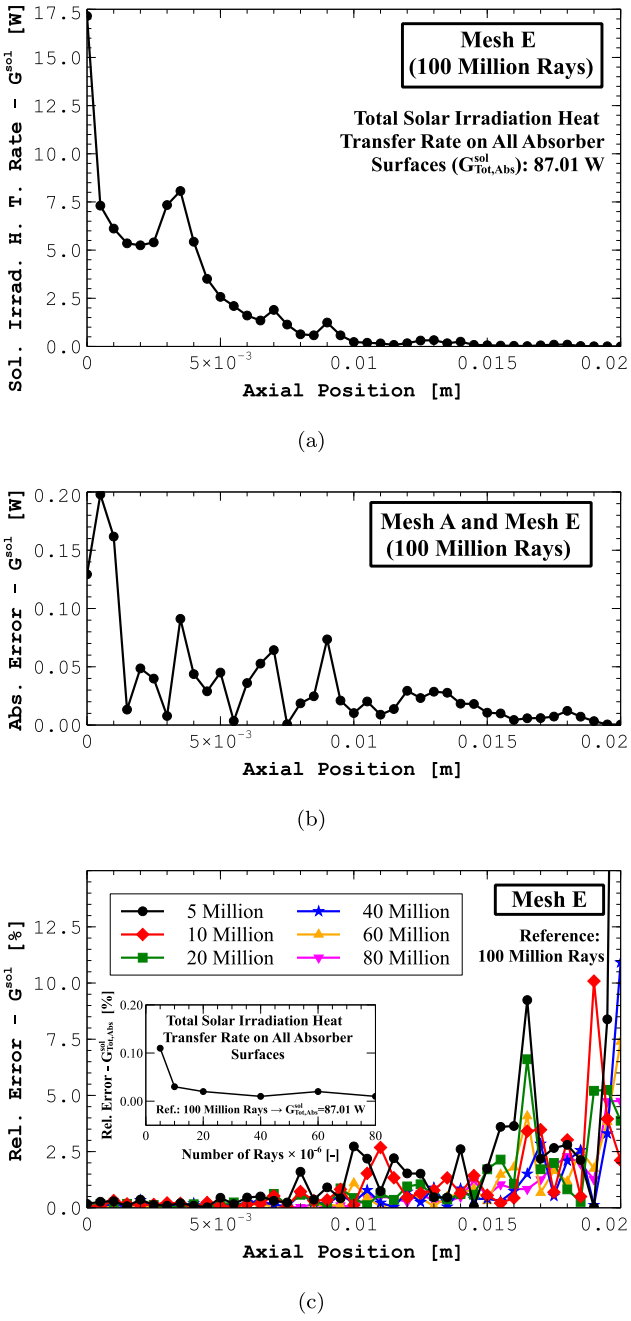

Fig. 13. Solar irradiation absorption by the absorber: (a) heat transfer rate profiles along the absorber axial direction computed with mesh E and 100 million rays; (b) absolute error of heat transfer rate profiles between mesh A and mesh E; and (c) relative errors of heat transfer rate profiles evaluated with mesh E and with different total numbers of rays in relation to the solution calculated with 100 million rays.

average relative errors decrease. For 80 million rays, the maximum and average relative errors are equal to 4.74% and 0.59%, respectively. The maximum relative error value is registered near the outlet absorber section. It is noteworthy that independently of the number of rays considered, the relative errors are more expressive in the absorber regions subjected to negligible solar radiation fluxes (i.e., although the relative errors are high, the absolute errors are small). The inset in Fig. 13c shows the relative error of the total solar irradiation heat transfer rate on all absorber surfaces for different total number of rays in relation to the results computed with 100 million rays. For 80 million rays the corresponding relative error is about 0.006%.

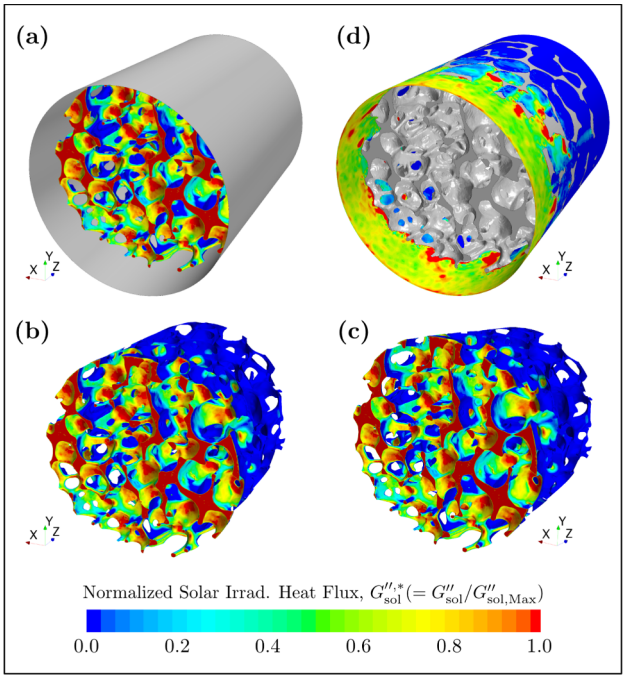

Fig. 14. Normalized solar irradiation heat flux distribution on the receiver walls: (a)–(c) absorber surfaces; and (d) receiver tubular surface. $G''_{sol,Max}$ is equal to 170 and 2 kW m^{-2} for cases (a)–(c) and case (d), respectively. Results computed with mesh E and with 100 million rays.

The receiver structure generated within the solar flux model framework based on the geometrical features of mesh E along with 100 million rays for performing MCRT model simulations was considered in this work for computing the solar flux distribution on the receiver surfaces, which is required for the receiver fluid flow and heat transfer model.

Figs. 14a–d exhibit the absorbed solar flux distribution on the receiver walls in a normalized fashion. Figs. 14a–c are concerned with the absorbed solar flux distribution on the absorber walls, whereas Fig. 14d addresses such distribution on the external receiver housing surface. Figs. 14a–c show the penetration of concentrated solar radiation through the pores of the volumetric absorber structure. This radiation becomes entrapped in the solid matrix. The highest solar irradiation heat flux values are observed at the inlet foam surface. Although not clearly shown, even at pore surfaces not directly irradiated by concentrated solar rays a non-negligible heat flux distribution is registered. This is particularly remarkable near the inlet section and is due to radiation reflection once the solar absorptivity of the cellular surface structure is not equal to one ($\alpha = 0.93$). Fig. 14d shows that the highest solar irradiation heat flux values on the absorber housing walls are noticed near the inlet section of the absorber. These high values are a consequence of radiation reflection from the foam skeleton and not primarily from direct concentrated solar radiation. (This evidence justifies the high angular (circumferential) irregularity of the absorbed heat flux at the receiver tubular wall.) Nevertheless, the heat transfer rate from (direct or reflected) concentrated solar radiation on this tubular surface is insignificant compared to the power registered on the absorber surfaces – see the normalization factor ($G''_{sol,Max}$) in the figure's caption.

Table 5 presents the heat transfer rate from concentrated solar insolation on different surfaces of the receiver. A total power over all receiver surfaces equal to 87.96 W is calculated. The tubular surface accounts for a negligible contribution of about 1% (0.95 W) on the total power. The power absorbed at the irradiated (front) absorber section (17.15 W) represents less than 20% of the total power absorbed by the overall foam structure surfaces. This value strongly supports that the

Table 5
Total absorbed heat transfer rates on the receiver walls from concentrated solar radiation exposure. Results computed with mesh E and 100 million rays.

Surfaces		Total Solar Irradiation Heat Transfer Rate [W]
Absorber walls		
	Inlet (front) surface	17.15
	Internal surface	69.86
	Total	87.01
Receiver tubular surface		0.95
Total receiver walls		87.96

surface approach – used in the literature to account for the concentrated solar radiation in the absorber energy model formulation through second-type boundary conditions (see, for instance, Refs. [17,36]) – may become unsuited for an accurate thermal and hydrodynamic performance prediction of the volumetric solar receiver. Due to the absorber internal pore structure and absorber length, a negligible fraction of the incident radiation escapes through the rear absorber section – negligible transmission losses (in full accordance with Fig. 13a which shows an insignificant fraction of incident radiation that is absorbed along the last few millimeters of the absorber). The power of the incident concentrated solar radiation at the receiver aperture (power-on-aperture, Q_0) is about 90.2 W (not shown in Table 5). For comparison purposes, if a planar disc surface with the same diameter as the receiver unit and with the same emissivity than that considered for SiC were placed at the receiver aperture section, the total absorbed power would be equal to about 83.90 W – about 5% less than the actual value of 87.96 W. Likewise, to absorb the same power as the current entire volumetric receiver, the planar disc surface would have to feature an apparent (effective) emissivity (ϵ_{appa}) of about 0.98 – instead of the intrinsic SiC surface value of 0.93. The different values between the discrete geometric definition for the receiver (current case) and the corresponding simplified definition (planar surface) support the evidence of a solar radiation entrapment effect in volumetric receiver applications [71].

The solar irradiation heat flux value on each boundary cell face of the mesh selected previously for receiver model simulations (mesh H-2 – see Section 5.1) is calculated by interpolating the values computed for mesh E. For the interpolated values on mesh H-2 in relation to the values computed for mesh E, a negligible relative error of the irradiation heat transfer rate on all receiver walls less than 0.56% is obtained. If the optical solution evaluated with mesh A were interpolated on the boundary cell faces of mesh H-2, the relative error of the total absorbed power would increase to about 3.27%. These values reinforce the selection of mesh E (instead of mesh A) for the solar flux model framework of simulations.

The optical efficiency of a concentrating solar collector system is defined as the ratio between the absorbed power by the receiver unit ($G_{sol,Rec}$) and the total incident power on the dish concentrator surface. Since a negligible shadowing effect on the concentrator surfaces due to the location of the receiver is expected – based on the area concentration ratio (less than 0.4%) – the total incident power on the dish concentrator surface can be evaluated as the product between solar flux (direct normal irradiation – q_s'') and the projected (aperture) area of the dish concentrator (A_{aper}). Therefore, the optical efficiency can be computed with Eq. (21). The optical efficiency accounts for energy losses due to radiation absorption on the concentrator surface (according to the actual value for ρ_{conc}), reflection on the receiver surfaces (ϵ_{appa}), and optical spillage (rays reflected from the concentrator that do not intersect the receiver – α_{spil} ($= 1 - Q_0/(q_s'' A_{aper} \rho_{conc})$). (Optical losses due to non-absorbed radiation at the absorber rear section – transmission losses – are negligible for the current absorber structure and incident concentrated solar radiation characteristics.) In alternative to Eq. (21), the optical efficiency can be computed as the product between ϵ_{appa}, ρ_{conc}, and $(1 - \alpha_{spil})$. The optical spillage losses from the receiver unit (α_{spil}) amount to about 20% of the total power reflected by the concentrator.

$$\eta_{opt} = \frac{G_{sol,Rec}}{q_s'' A_{aper}} \tag{21}$$

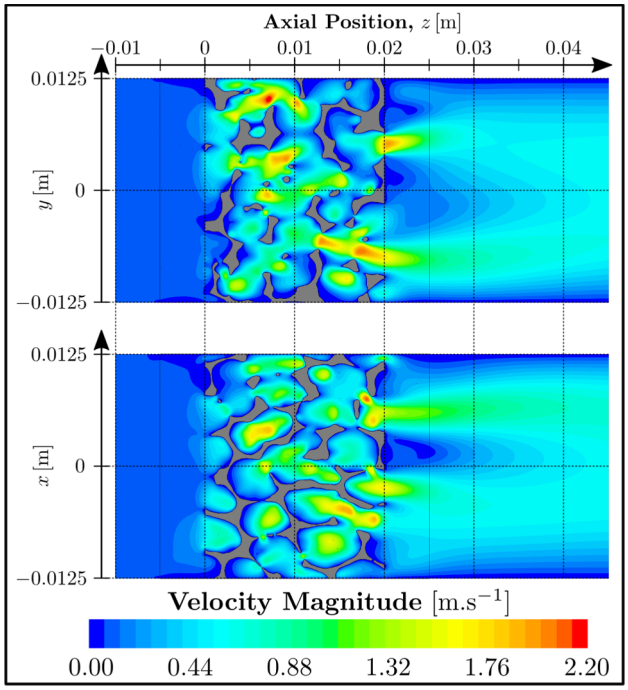

Fig. 15. Distribution of the fluid velocity magnitude field in two longitudinal cross-sections of the solar receiver. The absorber structure is located in $0 \leqslant z \leqslant 0.02$ m.

For the concentrating solar collector system under consideration, the optical efficiency is equal to about 70%.

Fig. 15 shows the distribution of the velocity magnitude on two perpendicular longitudinal cross-sections intersecting each other along the receiver centerline (symmetry axis). At the receiver walls, the application of no-slip boundary conditions is observed by a stagnant fluid layer adjacent to the walls. Local high velocity magnitudes are registered along the pore structure due to space confinement. Preferential fluid flow paths can be determined based on these results. Downstream the outlet section of the absorber structure (absorber's wake), highly uneven velocity magnitudes are noticed. The fluid velocity profiles tend to become parabolic-shaped along the receiver outlet manifold. The pressure drop along the receiver is equal to 3.63 Pa.

Fig. 16 shows the temperature distributions of the solid and fluid phases in different longitudinal and transversal cross-sections. Highly non-uniform temperature distributions – particularly, concerning the fluid phase – are observed in the first millimeters of the absorber. For the current operating condition, the solid and fluid phases are almost in thermal equilibrium 1 cm downstream the inlet absorber section. This evidence is in full agreement with the solar penetration depth observed in Fig. 13a.

Fig. 17 exhibits the surface temperature of the foam absorber. Slightly higher temperatures are observed in the middle-left surfaces of the absorber entrance region (near the receiver encasing wall). The maximum receiver surface temperature is registered in this region (ca. 1170 K). This hot-spot zone is the outcome of an imbalance between the heat transfer from this region to the adjacent fluid (and towards contiguous solid foam struts and upstream open environment) and the power absorbed from solar insolation. In this hot-spot region, the

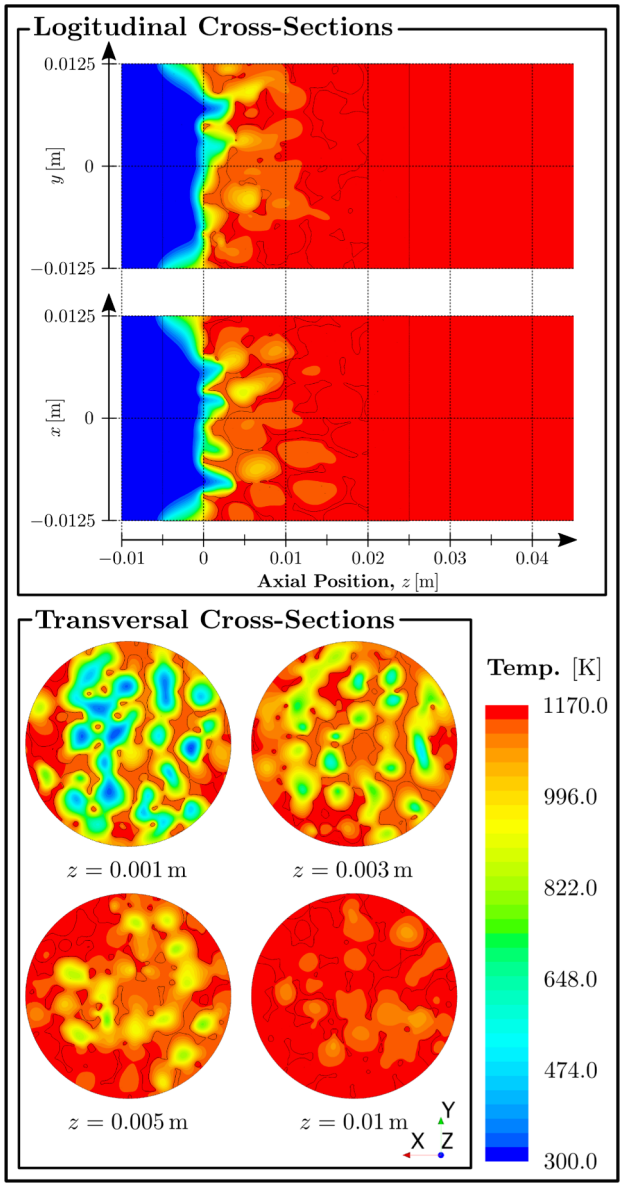

Fig. 16. Solid and fluid temperature distributions in longitudinal (top) and transversal (bottom) cross-sections of the solar receiver.

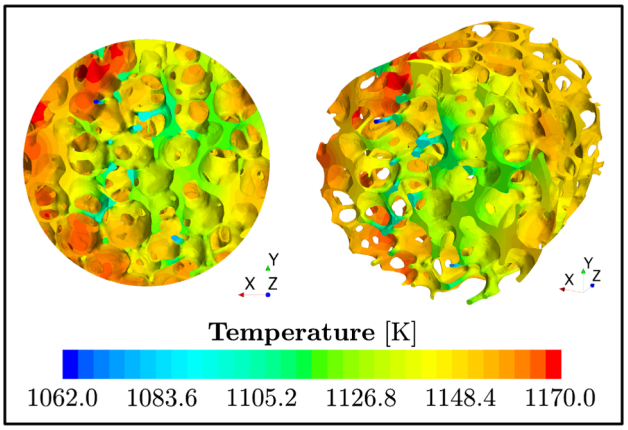

Fig. 17. Surface temperature of the absorber structure.

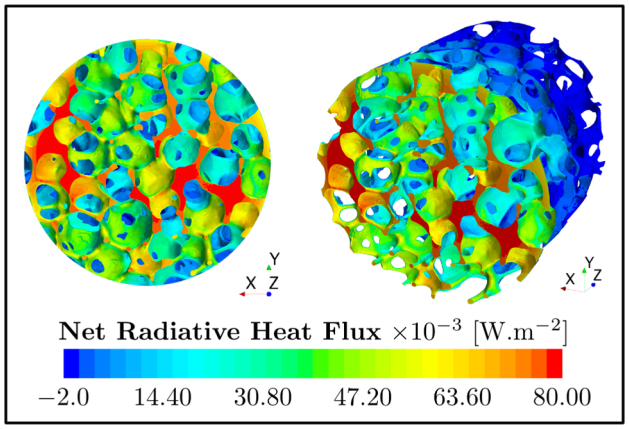

Fig. 18. Net radiative heat flux from thermal emission on the surfaces of the absorber structure.

absorber morphology is responsible for promoting deficient local fluid flow conditions leading to poor convective heat transfer rates in relation to the absorbed solar power. At the inlet section, the bare foam struts are at a significantly lower temperature because these surfaces have small areas exposed to concentrated solar radiation and, simultaneously, are in close contact with low fluid temperatures and high convective heat transfer coefficients.

Fig. 18 presents the net radiative heat flux on the surfaces of the absorber due to thermal emission. The surfaces at the absorber front face present the highest values of radiative heat flux once these surfaces are at a relatively high temperature and, mainly, because these surfaces are exposed to the surrounding (upstream) environment at 300 K. Albeit the surface temperatures are even higher further within the absorber unit than at the inlet section (see Fig. 16), the net radiative heat fluxes are lower within the absorber unit because the surrounding environment (absorber surfaces) is at a similar temperature and the optical thickness of the medium prevents heat exchange between absorber internal regions and upstream and downstream locations.

Figs. 19a–c present the average axial profiles for the velocity magnitude, gas and solid temperatures, and net radiative heat flux, respectively, along the receiver main flow direction. Fig. 19a shows that velocity magnitudes along the exit manifold are higher than at the receiver inlet manifold due to a higher temperature of the heat transfer fluid. (Neglecting pressure differences between upstream and downstream regions of the absorber, the velocity magnitude increase is equal to the ratio $T_{gas,out}/T_{gas,in}$, where $T_{gas,in}$ and $T_{gas,out}$ correspond to the HTF average temperatures at the inlet and outlet, respectively, receiver sections.) Fig. 19b reinforces the unsuitability of LTE models for an accurate prediction of the receiver performance. This is because at the inlet section of the absorber a significant difference between the solid and fluid mean temperatures (above 400 K) is established. The average fluid temperature increases even upstream the irradiated absorber section due to thermal conduction within the fluid phase. The solid and fluid temperatures achieve equilibrium as the distance from the irradiated absorber section increases. The average outlet gas temperature is about 1153 K. A moderate volumetric effect is observed under the current conditions since the average outlet fluid temperature (equal to the average rear solid temperature) is higher than the average front solid temperature ($T_{sol,in}$) – see the inset of Fig. 19b. The current ratio $T_{gas,out}/T_{sol,in}$ is about 1.02 – values up to 1.0325 were recently reported for a novel volumetric absorber structure investigated through a detailed experimental performance characterization [72]. Fig. 19c shows that thermal radiation is a significant mode of heat transfer throughout the first half of the absorber length and, consequently, should not be neglected. This evidence is in accordance with recent literature findings [73,74]. The radiative thermal (emission) losses are about 39.8% of the total absorbed power on the receiver unit. About 84.7% of the total

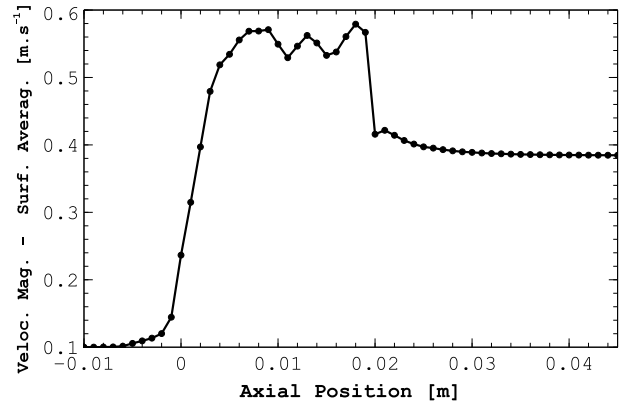

(a)

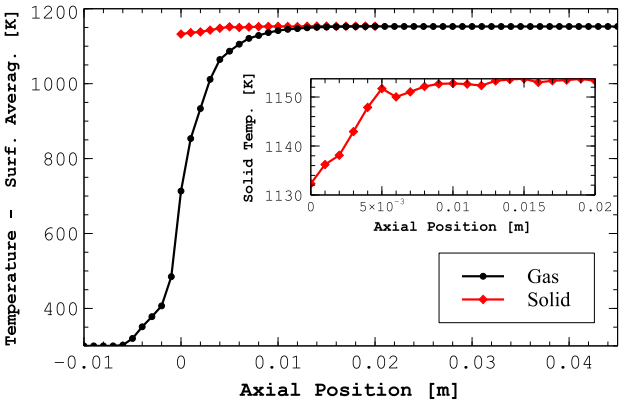

(b)

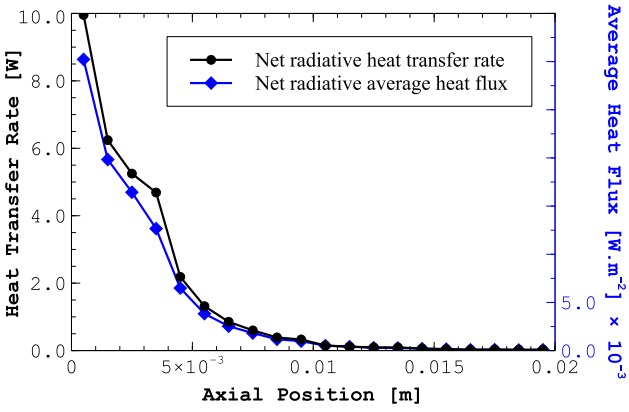

(c)

Fig. 19. Axial profiles of average velocity magnitude (a), average solid and gas temperatures (b), and net radiative heat transfer rate and average heat flux (c). The inset of (b) corresponds to the axial solid temperature profile.

radiative heat losses is emitted from the first 5 mm ($\approx d_{pore}$) of the ceramic foam absorber. The external tube (absorber housing) structure is responsible for a negligible contribution (about 5.6%) on the total emission losses.

The thermal performance of volumetric solar receivers is commonly evaluated through the calculation of the so-called solar-to-thermal energy conversion efficiency – shortly, thermal efficiency – according to Eq. (22). In this equation, Q_{fluid} is the power transferred from the receiver walls to the heat transfer fluid (useful thermal power). The thermal efficiency for the receiver under consideration is equal to about 59.0%.

$$\eta_{th} = \frac{Q_{fluid}}{Q_0} \tag{22}$$

The relatively small thermal efficiency value is in agreement with the high $Q_0/\dot{m}$ ratio – approximately equal to 1560 kJ kg^{-1}. The actual $Q_0/\dot{m}$ ratio and ensuing thermal efficiency value are within the common range of values found in literature (see, for instance, Refs. [75,76]). (However, because no experimental data is available matching the current operating conditions, geometrical parameters, and thermophysical properties – as far as the authors are aware –, any attempt to strictly compare the actual receiver thermal performance against a particular experimental data becomes inappropriate.) An increase in the thermal efficiency for the current receiver unit can be attained increasing the inlet fluid velocity – or decreasing the inlet fluid temperature (more impractical) – in such a way that an interfacial heat transfer enhancement between the solid and fluid phases is promoted which leads to a decrease of the absorber matrix temperature and, consequently, to a decrease of the thermal radiation losses. Alternatively, an increase in the thermal efficiency can be achieved by decreasing the receiver power-on-aperture, namely by redesigning the concentration system. These alternatives to increase the thermal efficiency have the side effect of decreasing the outlet fluid temperature which can penalize the performance of the downstream heat transfer fluid application. A simultaneous increase of the thermal efficiency and outlet fluid temperature can be obtained by considering improved absorber geometric and material properties.

6. Conclusion

The optical, hydrodynamic, and thermal performance characterization of an open volumetric air receiver for parabolic dish applications was herein carried out resorting to a comprehensive and state-of-the-art modeling procedure applied in the field of concentrating solar thermal energy research. The receiver hydrothermal performance was evaluated with discrete three-dimensional fully distributed pore-scale (direct) numerical simulation models. The fluid flow and heat transfer governing equations do not rely on external (empirical or theoretical) correlations and local convection heat transfer rates between solid and fluid phases are computed by solving the conjugate heat transfer problem. The absorbed solar flux distribution by the receiver internal reticulated surfaces was evaluated through the Monte Carlo ray tracing method taking into full consideration the role of the concentration system and the solar insolation characteristics. The three-dimensional absorber structure (ceramic open-cell foam) was obtained from computed tomography scans. A set of procedures was developed to generate the absorber geometrical model within the solar flux model framework and for coupling the solar flux model results with the receiver hydrothermal model. Best practice guidelines for consistent and accurate numerical predictions are provided. A mesh independence study on the absorber structure geometrical fidelity and on the receiver hydrothermal performance was conducted. The receiver and the solar flux models were validated against benchmark data. Considering the performance of a complete concentrating solar collector set, it was observed a solar radiation entrapment effect owing to the complex internal pore structure of the volumetric absorber. The thermal performance was within the typical experimental values registered in the literature. The volumetric effect was observed in this work.

The application of the current modeling approach allows to remarkably improve the accuracy of numerical predictions for the performance of volumetric solar absorbers. This is possible because the local (microscopic) receiver scales are resolved according to fundamental transport equations instead of being spatially averaged taking into account underlying assumptions. Consequently, the application of this methodology represents a great tool to improve the performance of concentrating solar collector systems and to shed light and gain

physical insight on open issues in the field of volumetric solar absorbers.

CRediT authorship contribution statement

Jorge E.P. Navalho: Conceptualization, Methodology, Software, Validation, Investigation, Writing - original draft, Writing - review & editing, Visualization. **José C.F. Pereira:** Supervision, Project administration.

Declaration of Competing Interest

The authors declare that they have no known competing financial interests or personal relationships that could have appeared to influence the work reported in this paper.

Acknowledgments

This work was supported by FCT, through IDMEC, under LAETA, project UIDB/50022/2020.

References

[1] Behar O, Khellaf A, Mohammedi K. A review of studies on central receiver solar thermal power plants. Renew Sustain Energy Rev 2013;23:12–39. https://doi.org/10.1016/j.rser.2013.02.017https://www.sciencedirect.com/science/article/pii/S1364032113001184.

[2] Pitz-Paal R. Chapter 19 – solar energy – concentrating solar power. In: Letcher TM, editor. Future energy 2nd ed.Boston: Elsevier; 2014. p. 405–31. https://doi.org/10.1016/B978-0-08-099424-6.00019-3http://www.sciencedirect.com/science/article/pii/B9780080994246000193.

[3] Baharoon DA, Rahman HA, Omar WZW, Fadhl SO. Historical development of concentrating solar power technologies to generate clean electricity efficiently – a review. Renew Sustain Energy Rev 2015;41:996–1027. https://doi.org/10.1016/j.rser.2014.09.008https://www.sciencedirect.com/science/article/pii/S1364032114007813.

[4] Müller-Steinhagen H, Trieb F. Concentrating solar power: a review of the technology. Ingenia 2004;18:43–50https://www.ingenia.org.uk/Ingenia/Articles/cb679c4f-9298-44aa-8356-ca9bff45704c.

[5] Lilliestam J, Labordena M, Patt A, Pfenninger S. Empirically observed learning rates for concentrating solar power and their responses to regime change. Nature Energy 2017;2:17094. https://doi.org/10.1038/nenergy.2017.94https://www.nature.com/articles/nenergy201794.

[6] Liu M, Tay NS, Bell S, Belusko M, Jacob R, Will G, Saman W, Bruno F. Review on concentrating solar power plants and new developments in high temperature thermal energy storage technologies. Renew Sustain Energy Rev 2016;53:1411–32. https://doi.org/10.1016/j.rser.2015.09.026https://www.sciencedirect.com/science/article/pii/S136403211500996X.

[7] Lilliestam J, Barradi T, Caldés N, Gomez M, Hanger S, Kern J, Komendantova N, Mehos M, Hong WM, Wang Z, Patt A. Policies to keep and expand the option of concentrating solar power for dispatchable renewable electricity. Energy Policy 2018;116:193–7. https://doi.org/10.1016/j.enpol.2018.02.014https://www.sciencedirect.com/science/article/pii/S0301421518300909.

[8] Gibb D, Johnson M, Roman J, Gasia J, Cabeza LF, Seitz A. Process integration of thermal energy storage systems evaluation methodology and case studies. Appl Energy 2018;230:750–60. https://doi.org/10.1016/j.apenergy.2018.09.001http://www.sciencedirect.com/science/article/pii/S0306261918313023.

[9] Lovegrove K, Pye J. 2 - Fundamental principles of concentrating solar power (CSP) systems. In: Lovegrove K, Stein W, editors. Concentrating solar power technology, Woodhead Publishing series in energy Woodhead Publishing; 2012. p. 16–67. https://doi.org/10.1533/9780857096173.1.16https://www.sciencedirect.com/science/article/pii/B9781845697693500029.

[10] Ávila Marín AL. Volumetric receivers in solar thermal power plants with central receiver system technology: a review. Sol Energy 2011;85(5):891–910. https://doi.org/10.1016/j.solener.2011.02.002https://www.sciencedirect.com/science/article/pii/S0038092X11000302.

[11] Kribus A, Gray Y, Grijnevich M, Mittelman G, Mey-Cloutier S, Caliot C. The promise and challenge of solar volumetric absorbers. Sol Energy 2014;110:463–81. https://doi.org/10.1016/j.solener.2014.09.035https://www.sciencedirect.com/science/article/pii/S0038092X14004757.

[12] Gomez-Garcia F, González-Aguilar J, Olalde G, Romero M. Thermal and hydrodynamic behavior of ceramic volumetric absorbers for central receiver solar power plants: a review. Renew Sustain Energy Rev 2016;57:648–58. https://doi.org/10.1016/j.rser.2015.12.106https://www.sciencedirect.com/science/article/pii/S1364032115014896.

[13] de la Beaujardiere J-FPP, Reuter HC. A review of performance modelling studies associated with open volumetric receiver csp plant technology. Renew Sustain Energy Rev 2018;82:3848–62. https://doi.org/10.1016/j.rser.2017.10.086http://www.sciencedirect.com/science/article/pii/S1364032117314533.

[14] Lee H-J, Kim J-K, Lee S-N, Kang Y-H. Consistent heat transfer analysis for performance evaluation of multichannel solar absorbers. Sol Energy 2012;86(5):1576–85. https://doi.org/10.1016/j.solener.2012.02.020https://www.sciencedirect.com/science/article/pii/S0038092X12000849.

[15] Zaversky F, Aldaz L, Sánchez M, Ávila-Marín AL, Roldán MI, Fernández-Reche J, Füssel A, Beckert W, Adler J. Numerical and experimental evaluation and optimization of ceramic foam as solar absorber – single-layer vs multi-layer configurations. Appl Energy 2018;210:351–75. https://doi.org/10.1016/j.apenergy.2017.11.003https://www.sciencedirect.com/science/article/pii/S0306261917315787.

[16] Avila-Marin A, Fernandez-Reche J, Martinez-Tarifa A. Modelling strategies for porous structures as solar receivers in central receiver systems: A review. Renew Sustain Energy Rev 2019;111:15–33. https://doi.org/10.1016/j.rser.2019.03.059https://www.sciencedirect.com/science/article/pii/S1364032119301996.

[17] Chen X, Xia X-L, Liu H, Li Y, Liu B. Heat transfer analysis of a volumetric solar receiver by coupling the solar radiation transport and internal heat transfer. Energy Convers Manage 2016;114:20–7. https://doi.org/10.1016/j.enconman.2016.01.074https://www.sciencedirect.com/science/article/pii/S019689041630022X.

[18] Avila-Marin AL, Caliot C, de Lara MA, Fernandez-Reche J, Montes MJ, Martinez-Tarifa A. Homogeneous equivalent model coupled with P1-approximation for dense wire meshes volumetric air receivers. Renewable Energy 2019;135:908–19. https://doi.org/10.1016/j.renene.2018.12.061https://www.sciencedirect.com/science/article/pii/S0960148118315052.

[19] Barreto G, Canhoto P, Collares-Pereira M. Three-dimensional CFD modelling and thermal performance analysis of porous volumetric receivers coupled to solar concentration systems. Appl Energy 2019;252. https://doi.org/10.1016/j.apenergy.2019.113433. 113433 https://www.sciencedirect.com/science/article/pii/S0306261919311079.

[20] Roldán M, Fernández-Reche J, Ballestrín J. Computational fluid dynamics evaluation of the operating conditions for a volumetric receiver installed in a solar tower. Energy 2016;94:844–56. https://doi.org/10.1016/j.energy.2015.11.035https://www.sciencedirect.com/science/article/pii/S0360544215015856.

[21] Gu R, Ding J, Wang Y, Yuan Q, Wang W, Lu J. Heat transfer and storage performance of steam methane reforming in tubular reactor with focused solar simulator. Appl Energy 2019;233–234:789–801. https://doi.org/10.1016/j.apenergy.2018.10.072https://www.sciencedirect.com/science/article/pii/S0306261918316404.

[22] Wu Z, Caliot C, Bai F, Flamant G, Wang Z, Zhang J, Tian C. Experimental and numerical studies of the pressure drop in ceramic foams for volumetric solar receiver applications. Appl Energy 2010;87(2):504–13. https://doi.org/10.1016/j.apenergy.2009.08.009https://www.sciencedirect.com/science/article/pii/S0306261909003122.

[23] Wu Z, Caliot C, Flamant G, Wang Z. Coupled radiation and flow modeling in ceramic foam volumetric solar air receivers. Sol Energy 2011;85(9):2374–85. https://doi.org/10.1016/j.solener.2011.06.030https://www.sciencedirect.com/science/article/pii/S0038092X11002428.

[24] Du S, He Y-L, Yang W-W, Liu Z-B. Optimization method for the porous volumetric solar receiver coupling genetic algorithm and heat transfer analysis. Int J Heat Mass Transf 2018;122:383–90. https://doi.org/10.1016/j.ijheatmasstransfer.2018.01.120https://www.sciencedirect.com/science/article/pii/S0017931017347853.

[25] Du S, Tong Z-X, Zhang H-H, He Y-L. Tomography-based determination of Nusselt number correlation for the porous volumetric solar receiver with different geometrical parameters. Renewable Energy 2019;135:711–8. https://doi.org/10.1016/j.renene.2018.12.001https://www.sciencedirect.com/science/article/pii/S0960148118314320.

[26] Xu C, Song Z, der Chen L, Zhen Y. Numerical investigation on porous media heat transfer in a solar tower receiver. Renewable Energy 2011;36(3):1138–44. https://doi.org/10.1016/j.renene.2010.09.017https://www.sciencedirect.com/science/article/pii/S0960148110004489.

[27] Wang P, Li J, Bai F, Liu D, Xu C, Zhao L, Wang Z. Experimental and theoretical evaluation on the thermal performance of a windowed volumetric solar receiver. Energy 2017;119:652–61. https://doi.org/10.1016/j.energy.2016.11.024https://www.sciencedirect.com/science/article/pii/S0360544216316309.

[28] Xia X, Chen X, Sun C, Li Z, Liu B. Experiment on the convective heat transfer from airflow to skeleton in open-cell porous foams. Int J Heat Mass Transf 2017;106:83–90. https://doi.org/10.1016/j.ijheatmasstransfer.2016.10.053https://www.sciencedirect.com/science/article/pii/S0017931016319214.

[29] Bianchi E, Heidig T, Visconti CG, Groppi G, Freund H, Tronconi E. An appraisal of the heat transfer properties of metallic open-cell foams for strongly exo-/endothermic catalytic processes in tubular reactors. Chem Eng J 2012;198–199:512–28. https://doi.org/10.1016/j.cej.2012.05.045https://www.sciencedirect.com/science/article/pii/S1385894712006171.

[30] Meinicke S, Wetzel T, Dietrich B. Scale-resolved CFD modelling of single-phase hydrodynamics and conjugate heat transfer in solid sponges. Int J Heat Mass Transf 2017;108:1207–19. https://doi.org/10.1016/j.ijheatmasstransfer.2016.12.052https://www.sciencedirect.com/science/article/pii/S0017931016323201.

[31] Li Z, Xia X, Li X, Sun C. Discrete vs. continuum-scale simulation of coupled radiation and convection inside rectangular channel filled with metal foam. Int J Therm Sci 2018;132:219–33. https://doi.org/10.1016/j.ijthermalsci.2018.06.010https://www.sciencedirect.com/science/article/pii/S1290072917314990.

[32] Capuano R, Fend T, Schwarzbözl P, Smirnova O, Stadler H, Hoffschmidt B, Pitz-Paal R. Numerical models of advanced ceramic absorbers for volumetric solar receivers. Renew Sustain Energy Rev 2016;58:656–65. https://doi.org/10.1016/j.rser.2015.12.068https://www.sciencedirect.com/science/article/pii/S1364032115014513.

[33] Dixit T, Ghosh I. Simulation intricacies of open-cell metal foam fin subjected to convective flow. Appl Therm Eng 2018;137:532–44. https://doi.org/10.1016/j.applthermaleng.2018.04.011https://www.sciencedirect.com/science/article/pii/

S1359431118300401.
[34] de Carvalho TP, Morvan HP, Hargreaves DM, Oun H, Kennedy A. Pore-scale numerical investigation of pressure drop behaviour across open-cell metal foams. Transp Porous Media 2017;117(2):311–36. https://doi.org/10.1007/s11242-017-0835-y.
[35] Mey-Cloutier S, Caliot C, Kribus A, Gray Y, Flamant G. Experimental study of ceramic foams used as high temperature volumetric solar absorber. Sol Energy 2016;136:226–35. https://doi.org/10.1016/j.solener.2016.06.066https://www.sciencedirect.com/science/article/pii/S0038092X1630247X.
[36] Wang F, Shuai Y, Tan H, Yu C. Thermal performance analysis of porous media receiver with concentrated solar irradiation. Int J Heat Mass Transf 2013;62:247–54. https://doi.org/10.1016/j.ijheatmasstransfer.2013.03.003https://www.sciencedirect.com/science/article/pii/S0017931013002081.
[37] Reddy K, Nataraj S. Thermal analysis of porous volumetric receivers of concentrated solar dish and tower systems. Renewable Energy 2019;132:786–97. https://doi.org/10.1016/j.renene.2018.08.030https://www.sciencedirect.com/science/article/pii/S0960148118309807.
[38] Villafán-Vidales H, Abanades S, Caliot C, Romero-Paredes H. Heat transfer simulation in a thermochemical solar reactor based on a volumetric porous receiver. Appl Therm Eng 2011;31(16):3377–86. https://doi.org/10.1016/j.applthermaleng.2011.06.022https://www.sciencedirect.com/science/article/pii/S1359431111003322.
[39] Wang F, Tan J, Yong S, Tan H, Chu S. Thermal performance analyses of porous media solar receiver with different irradiative transfer models. Int J Heat Mass Transf 2014;78:7–16. https://doi.org/10.1016/j.ijheatmasstransfer.2014.06.035https://www.sciencedirect.com/science/article/pii/S0017931014005079.
[40] Nakakura M, Bellan S, Matsubara K, Kodama T. Conjugate radiation-convection-conduction simulation of volumetric solar receivers with cut-back inlets. Sol Energy 2018;170:606–17. https://doi.org/10.1016/j.solener.2018.06.006https://www.sciencedirect.com/science/article/pii/S0038092X18305474.
[41] Fend T, Schwarzbözl P, Smirnova O, Schöllgen D, Jakob C. Numerical investigation of flow and heat transfer in a volumetric solar receiver. Renewable Energy 2013;60:655–61. https://doi.org/10.1016/j.renene.2013.06.001https://www.sciencedirect.com/science/article/pii/S0960148113002942.
[42] Chen X, Xia X, Dong X, Dai G. Integrated analysis on the volumetric absorption characteristics and optical performance for a porous media receiver. Energy Convers Manage 2015;105:562–9. https://doi.org/10.1016/j.enconman.2015.08.028https://www.sciencedirect.com/science/article/pii/S0196890415007748.
[43] Barreto G, Canhoto P, Collares-Pereira M. Three-dimensional modelling and analysis of solar radiation absorption in porous volumetric receivers. Appl Energy 2018;215:602–14. https://doi.org/10.1016/j.apenergy.2018.02.065https://www.sciencedirect.com/science/article/pii/S0306261918301922.
[44] Du S, Ren Q, He Y-L. Optical and radiative properties analysis and optimization study of the gradually-varied volumetric solar receiver. Appl Energy 2017;207:27–35. https://doi.org/10.1016/j.apenergy.2017.05.165. transformative Innovations for a Sustainable Future – Part II https://www.sciencedirect.com/science/article/pii/S0306261917307249.
[45] Kasaeian A, Barghamadi H, Pourfayaz F. Performance comparison between the geometry models of multi-channel absorbers in solar volumetric receivers. Renewable Energy 2017;105:1–12. https://doi.org/10.1016/j.renene.2016.12.038http://www.sciencedirect.com/science/article/pii/S0960148116310941.
[46] Cagnoli M, Savoldi L, Zanino R, Zaversky F. Coupled optical and CFD parametric analysis of an open volumetric air receiver of honeycomb type for central tower CSP plants. Sol Energy 2017;155:523–36. https://doi.org/10.1016/j.solener.2017.06.038https://www.sciencedirect.com/science/article/pii/S0038092X17305479.
[47] Ali M, Rady M, Attia MA, Ewais EM. Consistent coupled optical and thermal analysis of volumetric solar receivers with honeycomb absorbers. Renewable Energy 2020;145:1849–61. https://doi.org/10.1016/j.renene.2019.07.082http://www.sciencedirect.com/science/article/pii/S0960148119311024.
[48] Du S, Li M-J, Ren Q, Liang Q, He Y-L. Pore-scale numerical simulation of fully coupled heat transfer process in porous volumetric solar receiver. Energy 2017;140:1267–75. https://doi.org/10.1016/j.energy.2017.08.062https://www.sciencedirect.com/science/article/pii/S0360544217314408.
[49] Zhu Q, Xuan Y. Pore scale numerical simulation of heat transfer and flow in porous volumetric solar receivers. Appl Therm Eng 2017;120:150–9. https://doi.org/10.1016/j.applthermaleng.2017.03.141https://www.sciencedirect.com/science/article/pii/S1359431116324590.
[50] Capuano R, Fend T, Stadler H, Hoffschmidt B, Pitz-Paal R. Optimized volumetric solar receiver: thermal performance prediction and experimental validation. Renewable Energy 2017;114:556–66. https://doi.org/10.1016/j.renene.2017.07.071https://www.sciencedirect.com/science/article/pii/S0960148117306997.
[51] Yushkevich PA, Piven J, Hazlett HC, Smith RG, Ho S, Gee JC, Gerig G. User-guided 3D active contour segmentation of anatomical structures: significantly improved efficiency and reliability. NeuroImage 2006;31(3):1116–28. https://doi.org/10.1016/j.neuroimage.2006.01.015https://www.sciencedirect.com/science/article/pii/S1053811906000632.
[52] Petrasch J, Meier F, Friess H, Steinfeld A. Tomography based determination of permeability, Dupuit-Forchheimer coefficient, and interfacial heat transfer coefficient in reticulate porous ceramics. Int J Heat Fluid Flow 2008;29(1):315–26. https://doi.org/10.1016/j.ijheatfluidflow.2007.09.001https://www.sciencedirect.com/science/article/pii/S0142727X07001282.
[53] Dietrich B, Schabel W, Kind M, Martin H. Pressure drop measurements of ceramic sponges – determining the hydraulic diameter. Chem Eng Sci 2009;64(16):3633–40. https://doi.org/10.1016/j.ces.2009.05.005https://www.sciencedirect.com/science/article/pii/S0009250909003133.
[54] Modest MF. Radiative heat transfer. Academic press; 2013.
[55] Delatorre J, Baud G, Bézian J, Blanco S, Caliot C, Cornet J, Coustet C, Dauchet J, Hafi ME, Eymet V, Fournier R, Gautrais J, Gourmel O, Joseph D, Meilhac N, Pajot A, Paulin M, Perez P, Piaud B, Roger M, Rolland J, Veynandt F, Weitz S. Monte carlo advances and concentrated solar applications. Sol Energy 2014;103:653–81. https://doi.org/10.1016/j.solener.2013.02.035https://www.sciencedirect.com/science/article/pii/S0038092X13001448.
[56] White FM. Fluid mechanics. 8th ed. McGraw-Hill Education; 2016.
[57] Incropera FP, DeWitt DP, Bergman TL, Lavine AS. Fundamentals of heat and mass transfer. 6th ed. John Wiley & Sons; 2007.
[58] Munro RG. Material properties of a sintered α-SiC. J Phys Chem Ref Data 1997;26(5):1195–203. https://doi.org/10.1063/1.556000.
[59] Mao Q, Shuai Y, Yuan Y. Study on radiation flux of the receiver with a parabolic solar concentrator system. Energy Convers Manage 2014;84:1–6. https://doi.org/10.1016/j.enconman.2014.03.083https://www.sciencedirect.com/science/article/pii/S0196890414002945.
[60] Cunsolo S, Oliviero M, Harris WM, Andreozzi A, Bianco N, Chiu WK, Naso V. Monte carlo determination of radiative properties of metal foams: comparison between idealized and real cell structures. Int J Therm Sci 2015;87:94–102. https://doi.org/10.1016/j.ijthermalsci.2014.08.006http://www.sciencedirect.com/science/article/pii/S1290072914002312.
[61] Cunsolo S, Coquard R, Baillis D, Chiu WK, Bianco N. Radiative properties of irregular open cell solid foams. Int J Therm Sci 2017;117:77–89. https://doi.org/10.1016/j.ijthermalsci.2017.03.007http://www.sciencedirect.com/science/article/pii/S1290072916304379.
[62] Zhu Q, Xuan Y. Performance analysis of a volumetric receiver composed of packed shaped particles with spectrally dependent emissivity. Int J Heat Mass Transf 2018;122:421–31. https://doi.org/10.1016/j.ijheatmasstransfer.2018.02.006http://www.sciencedirect.com/science/article/pii/S0017931017344320.
[63] Mutuberria A, Monreal A, Albert A, Blanco M. Results of the empirical validation of Tonatiuh at Mini-Pegase CNRS-PROMES facility. Proceedings of the 17th international symposium on solar power and chemical energy systems. Granada, Spain: SolarPACES; 2011.
[64] Garrido GI, Patcas F, Lang S, Kraushaar-Czarnetzki B. Mass transfer and pressure drop in ceramic foams: a description for different pore sizes and porosities. Chem Eng Sci 2008;63(21):5202–17. https://doi.org/10.1016/j.ces.2008.06.015https://www.sciencedirect.com/science/article/pii/S0009250908003485.
[65] Dietrich B. Pressure drop correlation for ceramic and metal sponges. Chem Eng Sci 2012;74:192–9. https://doi.org/10.1016/j.ces.2012.02.047https://www.sciencedirect.com/science/article/pii/S0009250912001431.
[66] Di Benedetto A, Donsì F, Marra FS, Russo G. Heat and mass fluxes in the presence of fast exothermic superficial reaction. Combust Theor Model 2005;9(3):463–77. https://doi.org/10.1080/13647830500255296.
[67] Giani L, Groppi G, Tronconi E. Heat transfer characterization of metallic foams. Industr Eng Chem Res 2005;44(24):9078–85. https://doi.org/10.1021/ie050598p.
[68] Jeter SM. The distribution of concentrated solar radiation in paraboloidal collectors. J Sol Energy Eng 1986;108(3):219–25.
[69] Johnston G. Focal region measurements of the 20 m^2 tiled dish at the Australian National University. Sol Energy 1998;63(2):117–24. https://doi.org/10.1016/S0038-092X(98)00041-3https://www.sciencedirect.com/science/article/pii/S0038092X98000413.
[70] Lee H. The geometric-optics relation between surface slope error and reflected ray error in solar concentrators. Sol Energy 2014;101:299–307. https://doi.org/10.1016/j.solener.2013.12.035https://www.sciencedirect.com/science/article/pii/S0038092X14000024.
[71] Romero M, Steinfeld A. Concentrating solar thermal power and thermochemical fuels. Energy Environ Sci 2012;5:9234–45. https://doi.org/10.1039/C2EE21275Ghttps://pubs.rsc.org/en/content/articlepdf/2012/ee/c2ee21275g.
[72] Luque S, Menéndez G, Roccabruna M, González-Aguilar J, Crema L, Romero M. Exploiting volumetric effects in novel additively manufactured open solar receivers. Sol Energy 2018;174:342–51. https://doi.org/10.1016/j.solener.2018.09.030https://www.sciencedirect.com/science/article/pii/S0038092X18309022.
[73] Zhang H, Lougou BG, Pan R, Shuai Y, Wang F, Cheng Z, Tan H. Analysis of thermal transport and fluid flow in high-temperature porous media solar thermochemical reactor. Sol Energy 2018;173:814–24. https://doi.org/10.1016/j.solener.2018.08.015https://www.sciencedirect.com/science/article/pii/S0038092X18307849.
[74] Chen X, Wang F, Han Y, Yu R, Cheng Z. Thermochemical storage analysis of the dry reforming of methane in foam solar reactor. Energy Convers Manage 2018;158:489–98. https://doi.org/10.1016/j.enconman.2017.12.066https://www.sciencedirect.com/science/article/pii/S0196890417312189.
[75] Pitz-Paal R, Hoffschmidt B, Böhmer M, Becker M. Experimental and numerical evaluation of the performance and flow stability of different types of open volumetric absorbers under non-homogeneous irradiation. Sol Energy 1997;60(3):135–50. https://doi.org/10.1016/S0038-092X(97)00007-8https://www.sciencedirect.com/science/article/pii/S0038092X97000078.
[76] Fend T, Pitz-Paal R, Reutter O, Bauer J, Hoffschmidt B. Two novel high-porosity materials as volumetric receivers for concentrated solar radiation. Sol Energy Mater Sol Cells 2004;84(1):291–304. https://doi.org/10.1016/j.solmat.2004.01.039. international Solar Energy Society World Congress 2003 https://www.sciencedirect.com/science/article/pii/S0927024804001771.